NASA
Technical
Memorandum

NASA TM-86527

DE 1 RIMS OPERATIONAL CHARACTERISTICS

By R. C. Olsen, R. H. Comfort, M. O. Chandler, T. E. Moore, J. H. Waite, Jr., D. L. Reasoner, and A. P. Biddle

Space Science Laboratory
Science and Engineering Directorate

October 1985

National Aeronautics and
Space Administration

George C. Marshall Space Flight Center

MSFC - Form 3190 (Rev. May 1983)

TABLE OF CONTENTS page

LIST OF ILLUSTRATIONS

LIST OF ILLUSTRATIONS (Concluded)

TECHNICAL MEMORANDUM

DE 1 RIMS OPERATIONAL CHARACTERISTICS

I. INTRODUCTION

A. Philosophy

This manual is designed to aid new users of the Retarding Ion Mass Spectrometer (RIMS) data set to understand the data analysis process and the instrument characteristics. It is assumed that the reader is familiar with the basic characteristics of the RIMS sensor. Reference to the RIMS manual [1] is suggested for the uninitiated.

RIMS has significantly enhanced the capabilities of conventional ion traps and Retarding Potential Analyzers (RPAs) by separating the ions by mass and thus making available separate RPA and spin curves for each component species of the observed plasma. While in principle this simplifies the interpretation of the data, in practice additional complexities are introduced, primarily due to: (1) an energy dependent solid angle aperture resulting from acceleration of ions into the mass analyzer magnet to varying degrees, and (2) a finite energy bandwidth above the RPA potential, particularly in the high mass channel, where for the higher masses the energy band-width can be smaller than the RPA sweep range and narrower than some observed distributions. Under certain circumstances, these effects produce significant deviations from the response of conventional RPAs to hypothetical plasma distributions.

Craven and Reasoner [2] have considered the impact of these instrumental effects on the fitting procedure whereby plasma parameters are customarily inferred from RPA data [3]. In such a procedure, a drifting isotropic Maxwellian plasma described completely by a density, temperature, and drift (ram) velocity is assumed to exist outside a spacecraft sheath having some total potential drop. The response of the instrument to such a plasma is then computed as a function of RPA potential by appropriate integration of the distribution within the phase space boundaries taken to describe the aperture. Some authors [4,5] have chosen to map the ambient plasma inward through the sheath potential using the limits of integration appropriate to the aperture, while others [3] have chosen to map the aperture boundaries out-ward into the external plasma. The RPA potential is assumed to set a low-energy boundary beyond which the integral is evaluated to obtain a corresponding data pre-diction for each RPA value. An inference of all four parameters can be made using one RPA curve taken from the ram direction. The spin or Mach curve at zero RPA potential can be used to further constrain the parameters, particularly the ratio of drift to thermal speeds. Singh and Baugher [5] have shown that a thin sheath approximation is adequate for small angular apertures. Craven and Reasoner [2] have shown how to describe in phase space the energy-dependent solid angle aperture and the finite energy bandpass, and demonstrated the effects upon the inferred plasma parameters. The RIMS radial head has a narrow entrance aperture (20 deg) and mass resolution which for the first time makes possible the direct reduction of the data to physical quantities such as the ion intensity (differential directional flux) or phase space density. The RIMS data reveal many angular features which are inconsistent with the usual assumption of an isotropic Maxwellian plasma (e.g., loss cones and other symmetries about the local magnetic field). One approach to analyzing these features is to

fit a more complex distribution function to the data using theory as a guide. For example, theoretical predictions suggest that pronounced anisotropies should exist in such commonly observed phenomena as the polar wind. This approach has been demonstrated by Biddle et al. [6] who showed that observed asymmetries of polar wind spin curves can be fitted to a Maxwellian distribution corrected to first order for the presence of a heat flux according to the theory of Spitzer and Harm [7]. Other distributions such as bi-Maxwellians may also prove useful for certain types of data. Alternatively, it is possible to reverse this procedure and reduce the data directly to a measured distribution function. Procedures for this task are considered and demonstrated below.

B. Sketch of Approach

In general, conversion of a sensor count rate (CR) to a physical quantity such as intensity (I) or phase space density (f) requires the deconvolution of a response integral of the form:

$$CR = \int \mathrm{dE} \int d\Omega \int dA \ \mathrm{IR} \tag{1}$$

The limits of integration extend over the entire range of energy (E), solid angle (Ω) and entrance area (A). The variable R is a dimensionless function of position in the sensor entrance slit, the direction relative to the sensor look direction, and energy. R therefore describes the instrument response in area, solid angle, and energy. Note that I has dimensions [cm^{-2} s^{-1} sr^{-1} eV^{-1}] and is related to the phase space density as I = f (2E /m^2) . It is reasonable to assume that I is uniform over the sensor aperture, and that it may be removed from the integral, yielding:

$$CR = \int \mathrm{dE} \int d\Omega \ \ \mathrm{I} \ \ \mathrm{AR} \tag{2}$$

where

$$AR = \int dA \ \mathrm{R}$$

and A has dimensions of [cm^2] . In Section II various procedures are outlined for recovering I(E,phi) from CR(V_{rpa}, phi).

Note that I is the particle intensity at the sensor entrance, rather than in the ambient medium. Unambiguous conversion to ambient intensity requires a knowledge of the spacecraft potential for adjustment of the ion energy (Es = Ea + Φsc). The intensity can be adjusted according to Liouville's Theorem :

$$\mathrm{I_a(E_a) = I_s(E_s)\ E_a/E_s = I_s(E_s)(1 + (\Phi_{sc}/E_s)} \tag{3}$$

where the subscript a refers to ambient values and the subscript s refers to values at the sensor aperture. Alternatively, the sensor intensities may be converted to phase space densities which do not change in passing through the spacecraft sheath:

$$\mathrm{f_a\ (E_a = E_s + \Phi_{sc}) = f_s(E_s)} \tag{4}$$

For now it may be assumed that Φsc will be estimated or inferred by some independent means. Techniques for estimating (Φsc from the RIMS data are discussed below.

When the energy dependence of R defines a "window," as for a conventional electrostatic analyzer, one assumes that I has little variation within the window, removes it from the integral, and then simply solves for I in terms of the count rate and the integral energy response. When an RPA is used, defining a semi-infinite response function, the data must be differentiated or otherwise deconvolved with respect to energy (Fourier deconvolution, matrix inversion). The noise content of real data introduces problems with these procedures, which are discussed in more detail below.

II. IMPLEMENTATION FOR RIMS

A. Instrument Response Formulation

Consider a spherical coordinate system whose polar axis is aligned with the spacecraft spin axis and whose azimuthal reference meridian is defined to contain the spacecraft velocity vector. Polar and azimuthal angles in this system will be referred to as theta and phi, respectively. The convolution integral for a detector whose look direction is the spin phase angle (spa) may be written as:

$$CR\left(V_{rpa},spa\right) = \iiint I\, dE\, \sin(\theta)\, d\theta\, d\phi\, A \times R1(E,\theta,\phi) \times R2\left(E - V_{rpa}\right) \times EPS(E) \qquad (5)$$

where the integrals are over all energies and directions and:

1) I is the differential directional flux or intensity having dimensions [$cm^{-2}\ s^{-1}\ sr^{-1}\ eV^{-1}$] and is related to the phase space density by $I = f\,(2E/m^2)$.

2) R1 × R2 × AEPS is the composite response function, consisting of the following factors:

a) A is the effective area defined by the sensor aperture, determined by calibration of count rate against sources of known intensity. Dimensions are [cm^2] .

b) R1 is the energy dependent angular response function of the sensor. It is dimensionless with value unity in the center of the sensor look direction. The integral over angles yields the solid angle aperture defined by the sensor. R1 is found by calibration with a collimated monoenergetic source.

c) R2 is the energy response function. It is dimensionless and describes the region in energy space bounded at the lower limit by the retarding potential and at the upper limit by the response of the mass spectrometer channel in use. Ideally the energy response would extend well beyond the sweep range of the RPA potential. In general, this is true of the low mass channel but is not true of the high mass channel. This point is discussed below.

d) EPS is the detection efficiency function. It varies slowly with energy and nears unity when ions are preaccelerated to >2 keV prior to detection (as is the case in RIMS). It is therefore

adequate to lump EPS together with the constant A, to form AEPS, and it will be referenced as such below. In general, AEPS is a function of energy, but will be assumed to be independent of energy here. EPS may vary with time, as described below under inflight calibration.

B. Laboratory Calibration

Calibration consists of determining the response functions AEPS, R1, R2 by exciting the sensor with a laboratory ion beam which approximates a delta function in the integration variables E, θ, ϕ:

$$I = I_0 \ \delta \ \left(E\text{-}E_0, \sin(\theta\text{-}\theta_0), \phi\text{-}\phi_0\right), \tag{6}$$

so that:

$$CR\left(V_{rpa},spa\right) = I_0\left(AEPS\right) \ R1\left(E_0, \theta_0, \varphi_0\right) \ R2\left(E\text{-}V_{rpa}\right)$$

R2 is obtained by varying the magnet voltage for each mass peak rather than varying E0, since it is not practically possible to maintain constant source intensity while changing N. The effect is nearly the same for well-collimated beams. V_{rpa} is assumed to truncate R2 to the left at E = V_{rpa}. Two types of R2 functions result from the different modes of operation.

In the "default memory" mode, the mass analyzer magnet potential is held constant as V_{rpa} is swept. The result may be viewed as the product of the response for zero V_{rpa}, which we identify as R3(E); and a sliding step function which is written H(E-V_{rpa}). Each mass channel and species has a unique R3(E). The composite response is then R2(E,E- V_{rpa}) = H(E- V_{rpa})×R3(E), as illustrated in Figure 1.

In normal operating modes, the mass analyzer potential is decremented as the RPA potential is incremented, so that ions which just surmount the RPA obstacle fall at a constant position in the response function; i.e., R3 becomes R3(E- V_{rpa}), and

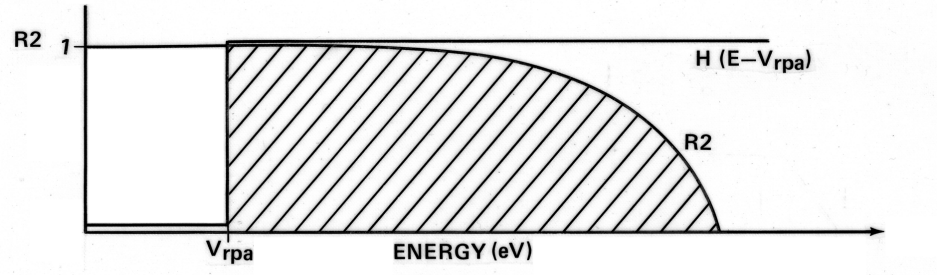

Figure 1. Energy response function with fixed R3, sliding V_{rpa}.

R2(E- V_{rpa}) = H(E- V_{rpa})xR3(E- V_{rpa}). In this case the necessity to convolve H and R3 disappears and there is one sliding response function R2 for each mass species and channel. RIMS may then be viewed as a differential analyzer with a broad response dependent upon the mass being observed as shown in Figure 2.

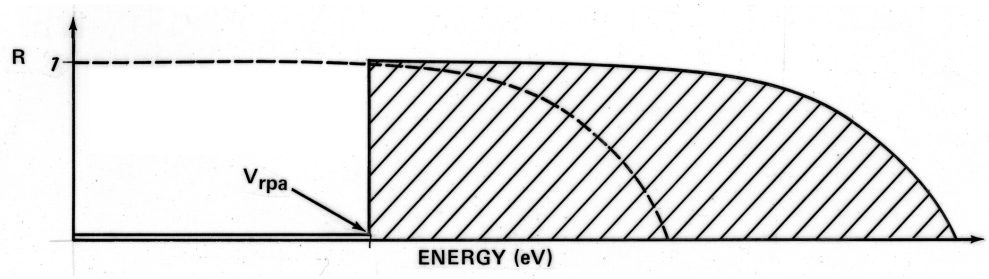

Figure 2. Energy response with sliding R3, V_{rpa}.

The above cases can be viewed as the convolution of an "ideal" RPA response H and a modified response R3, which has a fixed shape but can be a function of E or E- V_{rpa}, depending upon how the instrument is programmed. In practice R3 may be ignored for low mass channel data, since it is broad compared with the RPA sweep range. Unique R3s must be specified for each mass in the high mass channel and for each value of aperture bias. R3 has full widths of 14 eV and 51 eV for O+ and He, respectively, in the high mass channel and 64 eV and 256 eV for He+ and H+, respectively, in the low mass channel.

R1 is obtained by adjusting the magnet voltage for maximum R2, scanning the source over angular space, and then repeating at several energies. The energy-dependent angular response is thereby mapped. When integrating over distributions which vary weakly over the aperture, the following formulas result:

$$CR(V_{rpa},spa) = \int dE\ AEPS\ SA(E)\ R2(E,E-V_{rpa})\ I(E,spa) \quad (8)$$

Here, SA has the units of solid angle(sr) and is given by:

$$SA(E) = \iint \sin(\theta)\ d\theta\ d\phi\ R1(E,\theta,\phi) \quad (9)$$

Measured values of SA(E) for each head channel and mass are plotted in the RIMS manual [1].

C. Energy Response Deconvolution

With differential instruments, it is conventional to also assume that I is weakly varying over the energy response function. However, in the present discussion such an assumption will not be valid in general. With RPA instruments, it is conventional to assume that R2 is a step function H(E- V_{rpa}) and to view the measurements as integrals over all higher energy particles. This is not valid here for RIMS, particularly for the high mass channel, and a more sophisticated method of deconvolving the response integral is required.

The most rigorous approach to determining I in equation (5) is to treat the problem as one of solving an integral equation. In particular, equation (5) is of the type classified as a Fredholm

equation of the first kind with a displacement kernel (response function), and a semi-infinite integration domain; i.e., it is of the form:

$$g(x) = \int_0^\infty dy\ K(x-y)\ f(y) \tag{10}$$

It is straightforward to solve such an equation by means of Fourier transform techniques but highly consumptive of computer time for arbitrary kernel functions. Alternatively, the discreteness of the data may be utilized by writing the integral as a sum, in the form of a system of linear equations:

$$CR(V_{rpa}) = I(E)\ M(E, V_{rpa}) \tag{11}$$

The matrix M can be inverted to provide I directly from CR:

$$I(E) = CR(V_{rpa})\ M^{-1}(V_{rpa},E) \tag{12}$$

Where M = AEPS SA(E) R2(E, E-V_{rpa}) leads t the matrix values on a grid of energy versus RPA voltage. M^{-1} may be found for each species by standard inversion techniques which are implemented in an available FORTRAN subroutine:

$$M^{-1}_{ij} = \frac{\text{cofactor of } M_{ij}}{\text{determinant of } M}\ . \tag{13}$$

The matrix inversion technique appears promising, but has serious problems when the response function has no sharp structure in it, as when the RPA is not operating. It is still useful for quantitatively analyzing heavy ion data.

In cases where R2(E- V_{rpa}) is as wide or wider than the 0 to 50 V RPA sweep range (i.e., H+/low or He+/high), R2 may, to a good approximation, be regarded as a simple step function, as is customary (Fig. 3).

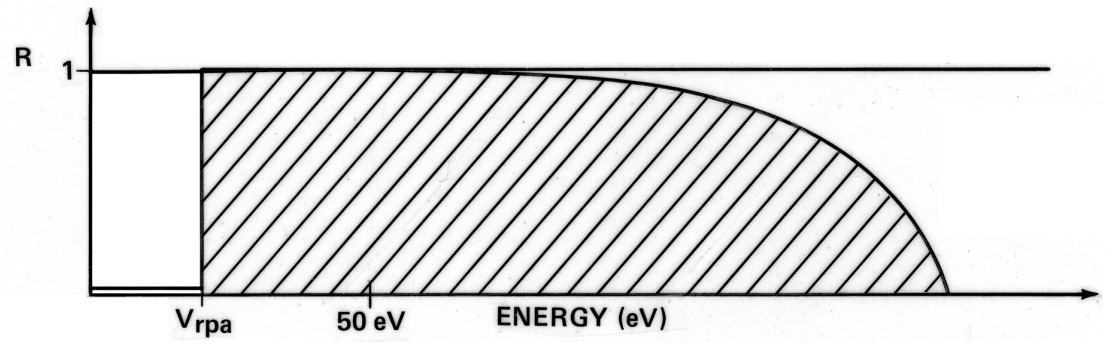

Figure 3. Similar to Figure 1 with width larger than 50 V V_{rpa} limit.

It is then possible to derive I(E) using a simple differencing technique:

$$DCR(V_{av},spa) = \int dE\ AEPS\ SA(E)\ R2(E,E-V_{rpa1})\ I(E,spa) - \int dE\ AEPS\ SA(E)\ R2(E,E-V_{rpa2})\ I(E,spa) \quad (14)$$

If a small interval, $V_{rpa\,1}$- $V_{rpa\,2}$ is used then I may be regarded as constant within it, and:

$$DCR(V_{av},spa) = q\ (V_{rpal}\ V_{rpa2})\ AEPS\ SA(E_{av})\ I(E_{av},spa)\ , \quad (15)$$

where V_{av} is the average value of V_{rpa} in the interval chosen, E_{av} is the corresponding energy, and q is the ion charge state. This provides an extremely simple and direct way of reducing the data which is always valid for the low mass channel and may be marginally valid for the high mass channel when it is set for He+.

This procedure has been implemented in the form of a subroutine, DIFRPA, which accepts as inputs an RPA curve data file together with information concerning the RIMS head, channel, and mass of the data. DIFRPA then returns to the calling routine a revised set of data in one of three forms:

1) The differential directional intensity [$cm^{-2}s^{-l}sr^{-l}eV^{-1}$] versus the center energies of the bins defined by the original RPA steps.

2) The phase space density [s^3km^{-6}] versus the center energies.

Or

3) The reconstructed integral flux [$cm^{-2}s^{-l}sr^{-l}eV^{-1}$] curve for the original data, with energy-dependent solid angle response applied.

An example of the results of this procedure is shown in Figure 4. The lower panel is a contour plot of count rates in a two-dimensional grid of retarding potentials and spin phase angles. The panel at the right indicates corresponding pitch angles relative to the magnetic field. In the upper panel, the differencing technique has been used to generate phase space densities at the instrument aperture. The noisiness of these numbers at energies below about 0.7 eV is due to the uncertainties of differentiating along the flat part of the RPA curves.

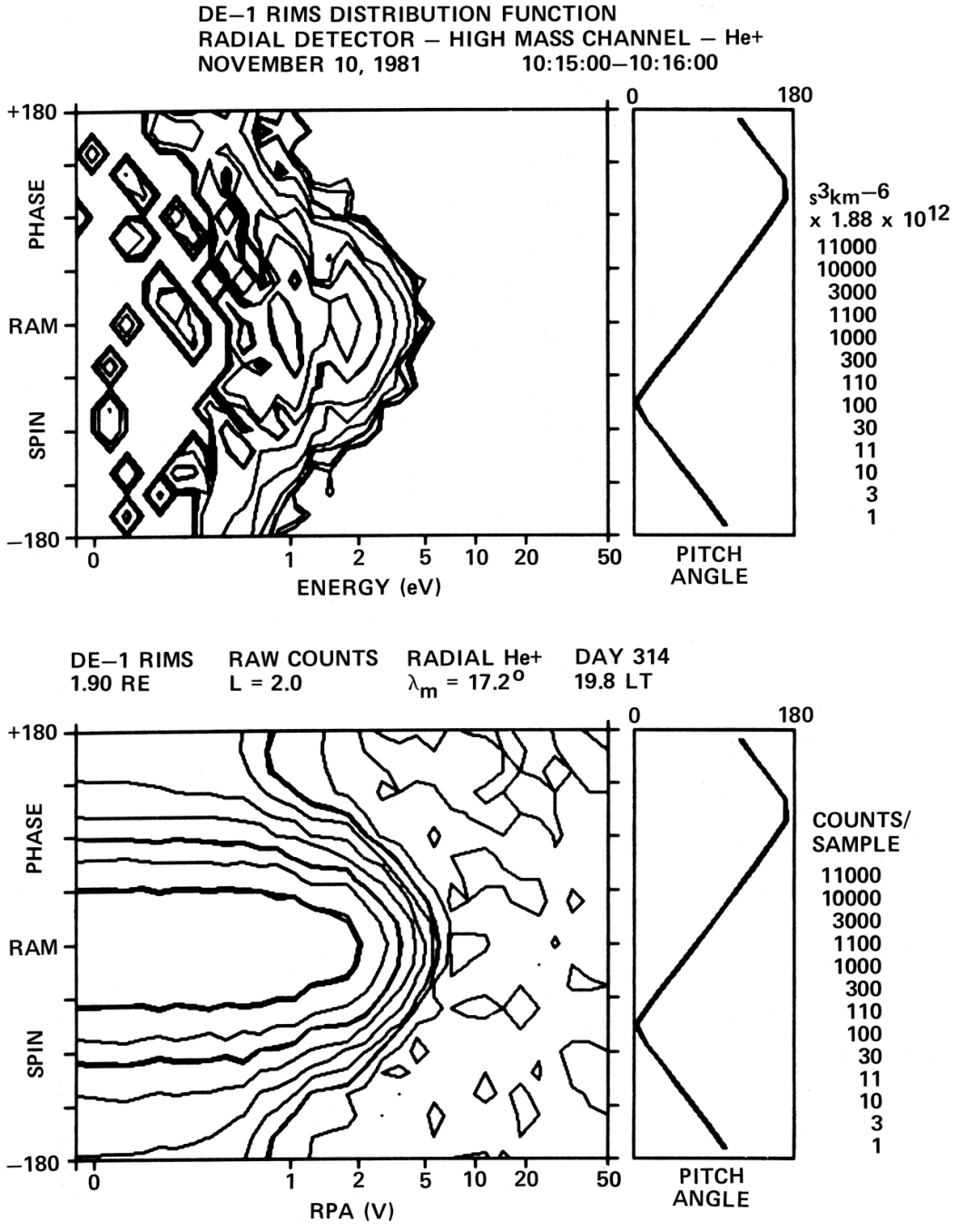

Figure 4. Direct reduction of He+ count rates (lower panel) to phase space densities (upper panel) by the differencing technique.

In the case of heavier ions such as O+, the differential response of RIMS is sufficiently narrow (approximately 14 eV FWHM) that the count rates may be processed as differential intensities using a constant energy bandwidth:

$$CR(V_{rpa},spa) = \int dE\ AEPS\ SA(E_{av})\ I(V_{rpa},spa) \tag{16}$$

where dE is the energy bandwidth of the O+ channel, E_{av} is the center energy of the channel (higher than V_{rpa} by dE/4), and V_{rpa} labels the mass slide sweep step whether or not the RPA is actually operating. An example of a cold rammed O+ distribution converted to phase space densities by this technique is shown in Figure 5.

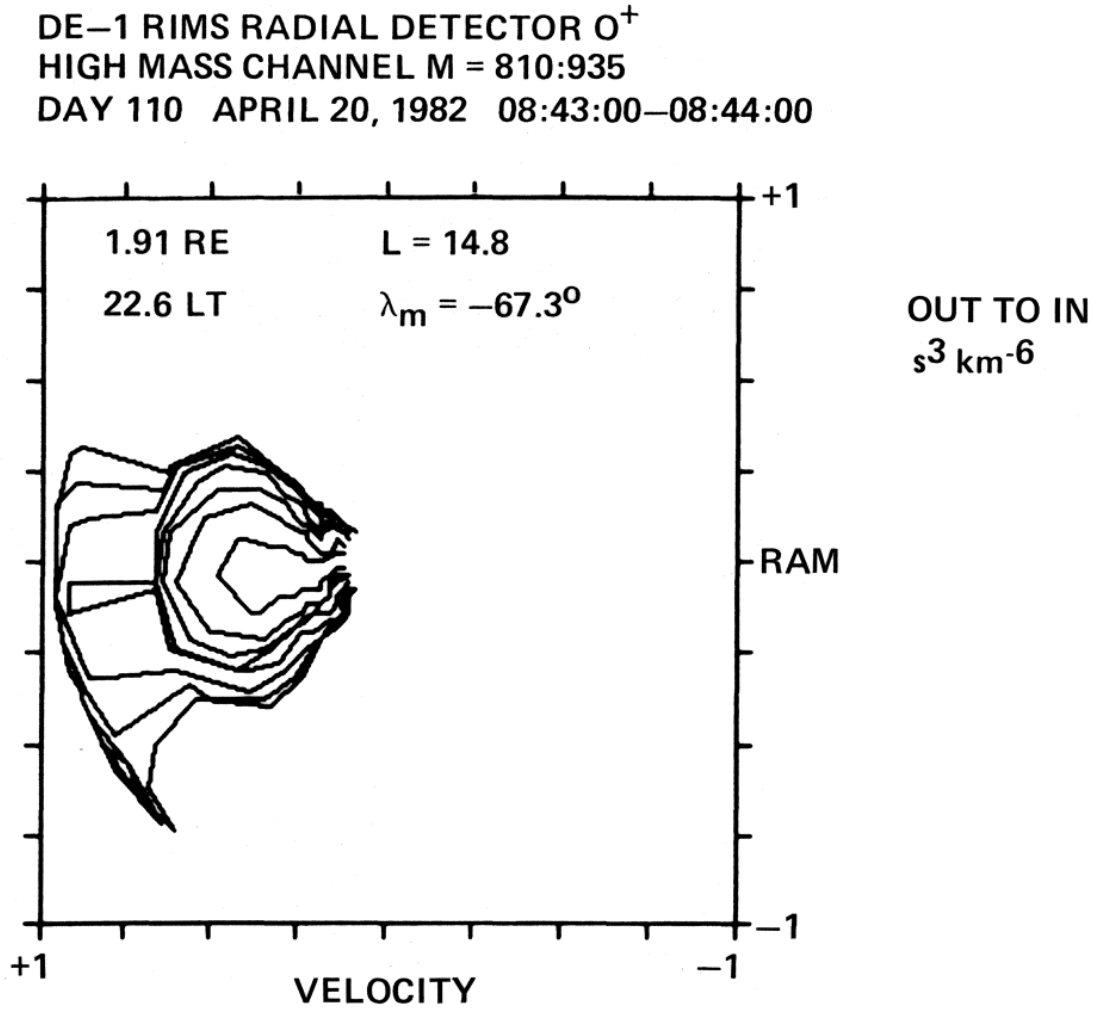

Figure 5. Cold rammed O+ distribution function in space velocity coordinates with full scale velocity corresponding to 50 eV O+ (24 km is). Contours are separated by a factor of approximately 2.0.

D. Conversion to Ambient Quantities (Sheath Mapping)

Use of the above procedure accounting for the instrument's measured response will yield the intensity or phase space density at the sensor aperture. However, it is also necessary to derive the distribution function or phase space densities in the ambient plasma around the spacecraft. The major effect to be considered is the floating potential of the spacecraft, which accelerates the plasma particles prior to their impact upon the spacecraft or sensor aperture. This acceleration has strong focusing effects upon those ions having ambient energies comparable with the spacecraft floating potential. However, intensities or phase space densities may be mapped very simply outward to the ambient phase space by means of Liouville's theorem, assuming that the sheath normal is parallel to the sensor look direction. This assumption is fairly well justified for the RIMS radial head, at least as projected into the spin plane, but not justified for the Z heads. The latter are mounted near the edge of the spacecraft disc and consequently look through a sheath which is tilted with respect to the spin axis, resulting in spin modulations when anisotropies are present.

The use of Liouville's theorem was summarized in the introduction in equations (3) and (4). Note that detected intensities (fluxes) differ significantly from ambient values only for ambient energies on the order of the spacecraft potential. The effect of the angular focusing is simply to narrow (widen) the angular resolution of the sensor for repulsive (attractive) spacecraft potentials. The main problem with positive potentials is the inability to observe the low speed parts of velocity space. Further, when the sheath normal is not parallel to the sensor look direction, as is the case for the Z heads of RIMS, the response direction is deflected from the look direction away from (toward) the sheath normal for repulsive (attractive) spacecraft potentials, the deflection depending inversely upon energy. The latter is a highly undesirable situation, difficult to avoid in practice, but can be minimized by symmetric mounting geometries.

A larger problem lies in the determination of the spacecraft potential. It is assumed above that a value is given. Unfortunately it is difficult to determine the potential from the ion observations without prior assumptions about the nature of the ion distribution. One possible exception is a case in which statistically significant intensities are recorded in all directions above a clearly defined minimum energy. In this case a negative potential may be inferred. Such cases may be rare due to the presence of trapped ion populations whose source is within the sheath (see Figure 4 for an example indicating a negative potential of approximately 0.5 V).

In the case of positive (repulsive) potentials, part of the ambient population cannot be observed, and there are no lower energy cutoffs expected. The RIMS aperture bias can demonstrably overcome this problem to some extent although the possibility of potential barriers forming in the complex spacecraft sheath still remains. It may be that a given bias results in the appearance of a lower energy cutoff, indicating an effective negative, potential for the RIMS sensor. Care must be taken that the cutoff exists in all look directions and is not the result of the high energy of a supersonic flow of cold plasma. Densities low enough to produce positive potentials are often constituted of supersonically flowing ions.

It is clear from the preceding discussion that future plasma investigations should have some self-contained method of determining the spacecraft potential, as well as aperture bias to overcome potentials which exist. Active spacecraft potential control using controlled plasma injections which maintain sheath symmetry would be useful as well.

E. Fitting Procedures

Quantitative analysis of RIMS data to determine temperature, density, and spacecraft potential may be carried out by fitting the data for a single ion species to model curves. For fitting RPA data, the thin sheath model for flux to a limited aperture RPA, derived by Comfort et al. [3] , is employed. The application of this model to the analysis of RIMS data is described in some detail by Comfort et al. [8]. The analysis procedure and the computer code which implements it have been modified to include fits to the spin curve for unretarded RPA data. This modification has not yet been documented in the literature.

The thin sheath model is formulated in terms of three dimensionless (unknown) variables, L, Vo, M, and a normalization factor, Fo, as defined in Figure 6. The equivalent set of (unknown) physical variables is T_i, N_i, $\phi_{s/c}$ and V_s. The relative velocity V_s is taken to be the negative of the spacecraft velocity ; effects of this approximation are discussed at length in Comfort et al. [8]. Density N_i is computed from the magnitude of the unretarded count rate in the ram direction. This leaves the temperature T_i and spacecraft potential cps/c to be determined from the RPA and spin curve shapes.

$$F_D = F_O \left\{ e^{-(L-M)^2} + \sqrt{\pi}\, M\, [1 - \mathrm{ERF}\,(L - M)] - \cos^2\theta_p\, e^{(Vo\ \mathrm{TAN}^2\theta_p - M^2 \sin^2\theta_p)} \left\{ e^{-(L\sec\theta_p - M\cos\theta_p)^2} + \sqrt{\pi\, M\cos\theta_p}\, [1 - \mathrm{ERF}\,(L\sec\theta_p - M\cos\theta_p)] \right\} \right\}$$

WHERE

$M^2 \equiv \tfrac{1}{2} M_i V_s^2 / k\, T_i$ = ION MACH NUMBER

$L^2 \equiv V_G + V_O$ $\quad (L = O \text{ FOR } V_G + V_O \leqslant)$

$V_G \equiv e\, \phi_{RPA} / kT_i$

$V_o \equiv e\, \phi_{S/C} / k\, T_i$

$F_o \equiv N \sqrt{kT_i / 2\pi M_i}$

$\Theta_p \equiv$ ACCEPTANCE ANGLE OF DETECTOR (CIRCULAR APERTURE)

Figure 6. Flux from a flowing Maxwellian ion distribution into a limited aperture RPA-thin sheath approximation.

In principal, the RPA curve alone is sufficient to determine both T_i and $\phi_{s/c}$. An iterative technique has been employed which fixes $\phi_{s/c}$ and fits the thin sheath model for T_i, then using the resulting value for T_i fits for$\phi_{s/c}$. This procedure is continued until there is convergence to unique values of T_i and $\phi_{s/c}$. For simulated data covering the range of values expected in and near the plasmasphere, this technique works quite satisfactorily, always converging to values within a few

percent of the correct ones, if sufficiently tight convergence tests are used, particularly for positive $\phi_{s/c}$ (see results and discussion of simulation calculations in Comfort et al. [3]).

For real data a disquieting behavior is encountered. For positive $\phi_{s/c}$, the iterative procedure frequently does not converge in the loop fitting for $\phi_{s/c}$; rather $\phi_{s/c}$ grows without limit, resulting in larger N_i. The cause of this lack of convergence is not known. It has been found that the minimum value of a positive $\phi_{s/c}$ typically occurs after the first loop fitting for $\phi_{s/c}$, so this value has been used with the recognition that it represents a lower limit. Clearly this state of affairs is not entirely satisfactory.

When it became possible to model spin curves in the thin sheath approximation (using empirical fits to numerically computed spin curves) as functions of Mach number (M) and (normalized) spacecraft potential (Vo), it became feasible to incorporate the spin curve data into the analysis as an independent source of information. It has been found that the RPA curve is quite sensitive to Ti and less so to $\phi_{s/c}$ while the spin curve appears to be equally sensitive to both. For this reason the iterative procedure presently employed uses the RPA curve to fit for temperature and the spin curve to fit for $\phi_{s/c}$. Since the fitting procedure for the RPA curve still produces a new value for $\phi_{s/c}$, it is possible to see the consistency (or lack thereof) between the two curves, as in Figure 7. Agreement is generally within about 10 to 20 percent for resulting densities, although percentage differences in $\phi_{s/c}$ may be larger. Here again, this discrepancy is associated with the data and not the technique; simulated data produce consistent results within 1 percent.

Because this revised technique depends on the spin curve, it is not applicable to Z head data. Analysis of Z head data is presently performed with the previous version of the program, although it is not as accurate as the analysis for radial head data. Comparisons of simultaneous radial and Z head data have shown good agreement in temperature, but systematic differences in densities. The end head indicates higher densities, particularly at lower altitudes. This may be associated with end head anomalies discussed elsewhere in this document.

F. Determination of the Field-Aligned Velocity and Flux

Determination of field-aligned velocity and flux is based on a simple technique involving the average flow velocity direction and a knowledge of the ram velocity and the convection velocity. The technique depends on the geometry of the DE 1 orbit (specifically the relationship of the satellite velocity vector to the magnetic field vector). The DE 1 orbit plane is very nearly (<10 deg) parallel to planes of constant magnetic longitude, enabling the RIMS radial head to sample almost all pitch angles in each spin. In order to measure the naturally occurring field-aligned flow velocity, it is necessary to first determine the direction of the total velocity vector, V_T, of the plasma (Fig. 8). Subtracting the satellite ram vector from this vector will leave, in general, a combination of flow vectors which result from three separate mechanisms; corotation, convection, and magnetic field-aligned flow.

The differential flux of ions, dJ, into the instrument is a function of the ion velocity, V, and the look direction of the instrument, defined here by the spherical coordinates theta and phi where theta is zero along the +Z axis of the spacecraft and phi is in the direction of the spin phase angle, i.e.:

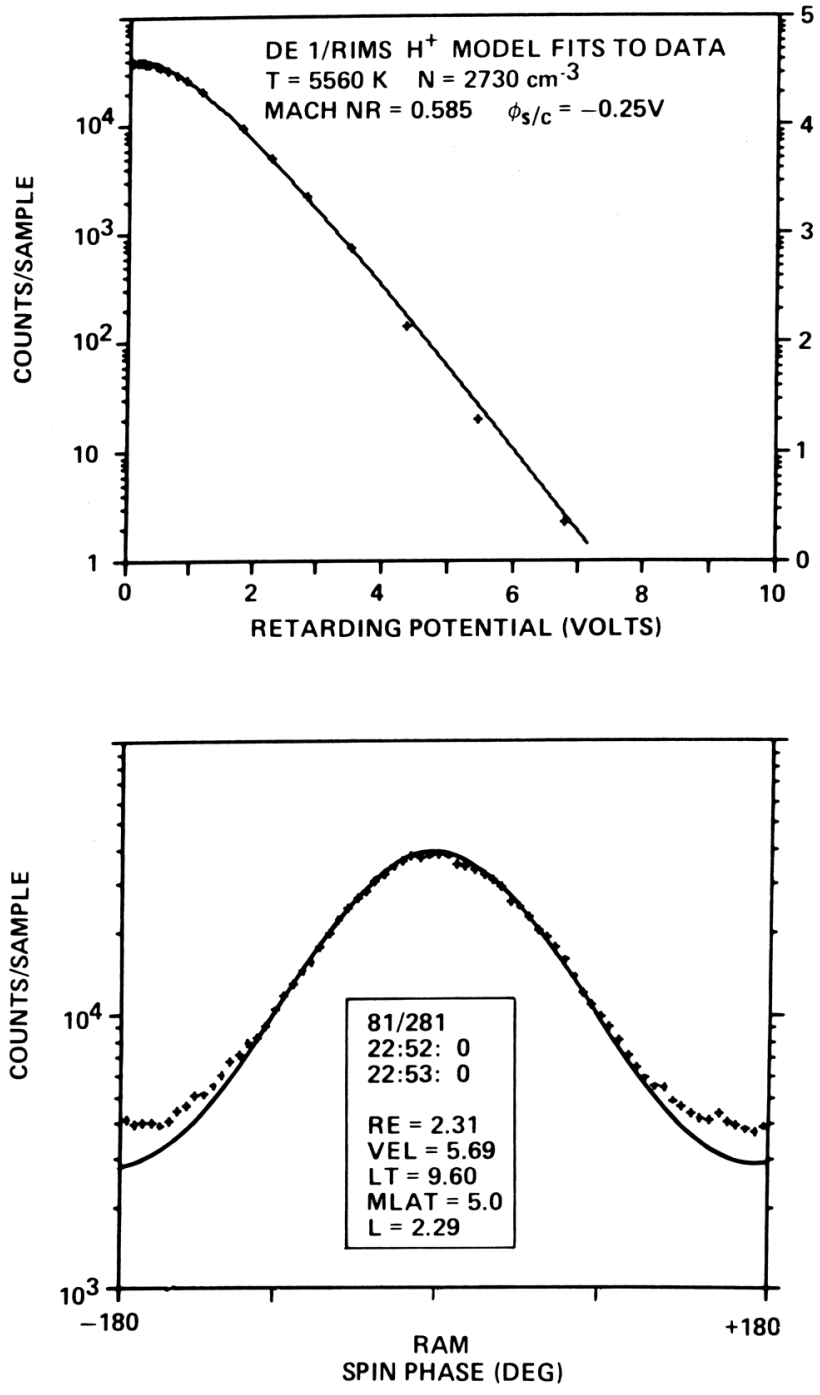

Figure 7. Sample RPA and spin curves showing Maxwellian fits to the data.

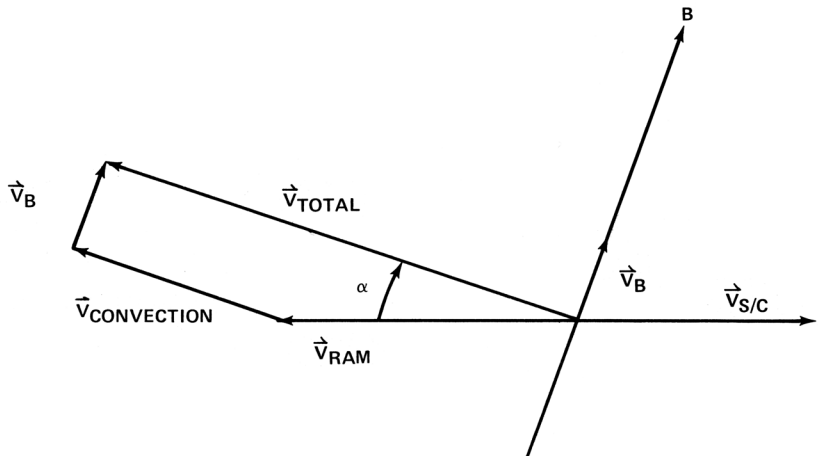

Figure 8. Geometry for derivation of bulk flow from integral flux spin curves.

$$d\vec{J} = \vec{F}(\theta,\phi,V) \tag{17}$$

To determine the average ion velocity components, $d\vec{J}$ must be integrated over all velocities and all directions. For an integral detector such as RIMS, the integral over the magnitude of the velocity is done by the instrument. In addition, since RIMS has an aperture width in the theta direction of 50 deg FWHM, the integration over theta is also carried out by the instrument. The final integration is,

$$\vec{J} = \int \vec{F}(\phi)\, d\phi \tag{18}$$

where F(q)) is the quantity measured by RIMS. For a single population,

$$\vec{J} = n\int \vec{V}_T(\phi)\ \ d\phi\ =\ n\left\langle \vec{V}_T \right\rangle \tag{19}$$

where VT includes all naturally occurring velocity components as well as the satellite ram velocity. VT can be broken into components along the spacecraft x and y axis. From these two components the direction of VT can be found, i.e.:

$$\tan(\phi_o) = \frac{n\left\langle \vec{V}_{Ty} \right\rangle}{n\left\langle \vec{V}_{Tx} \right\rangle} \tag{20}$$

where ϕ_0 is the angle from the spacecraft x axis to V_T. Given the direction of B and VT along with values of V_{ram} and V_{conv} the velocity along B is given by,

$$|\vec{V}_B| = \frac{V_{ramy} - V_{ramx} \tan \phi_0}{\sin \phi_B - \tan \phi_0 \cos \phi_B} \tag{21}$$

where ϕ_B is the angle of B with respect to the x axis. V_T can then be found from either equation (3) or (4). A lower limit density is defined by,

$$n = \frac{\int F(\phi)\ \cos(\phi - \phi_o)\ d\phi}{V_T} \tag{22}$$

and the flux along B is given by

$$\left|\Phi_B\right| = n\ \left|\vec{V}_B\right| \tag{23}$$

Some assumptions are made in this analysis. Because the DE 1 orbit is so nearly along a constant magnetic longitude, the effects of corotation are ignored. Unlike corotation, convection velocities resulting from east-west electric fields are in the spin plane and cannot be distinguished from field-aligned velocities by this technique. Therefore some knowledge of the convection velocity is necessary to determine the field-aligned component. There are three options available for specifying the convection velocity. They are :

1) A constant convection velocity specified at the satellite;

2) A constant electric field specified at 400 km which is mapped, under the assumption of a dipole magnetic field, to the satellite position; or

3) A data file containing values of the convection electric field as a function of time.

Option 2 is, in general, the best approach and has been used whenever good quality electric field data can be obtained from the Plasma Wave Instrument on DE 1. Error estimates indicate that the velocity determination is good to less than 0.10 km /s. The approximate values of flux and density given by equations (22) and (23) are only estimates. They do not include effects from non-zero spacecraft potentials and can only approximate the flux above an energy equivalent to this potential. For more details on this technique and the error estimates, see Chandler and Chappell [9].

G. Summary of Techniques, Applicability

The preceding discussion has identified various techniques for directly deriving fluxes and phase space densities from RIMS data. Due to the mixed integral/differential response of the RIMS sensor, the appropriate technique is dependent upon specific circumstances, i.e., mass, channel, head, and instrument operating mode. This section is an attempt to provide the casual RIMS data analyst with a "road map" of recommended procedures for analyzing the data.

1. Identifying periods of interest. It is usually sufficient to work with the summary retarding potential and spin spectrograms available on fiche to determine periods of interest for a given data study. There is no substitute for familiarity with the fiche format and the morphology visible in the fiche for this purpose. However, it should be noted that much detail present in the full data set is not evident in the spectrograms.

2. Identifying the type of analysis desired. When focusing upon particular data intervals, a bewildering array of possibilities presents itself. If there is reason to believe that the ion distributions are flowing Maxwellians, or Maxwellians modified by magnetic field-aligned heat flux, then it is sufficient to generate RPA curves in the apparent ram direction and/or zero retarding potential spin curves for the species of interest. This corresponds to quantitatively plotting individual strips from the retarding potential and spin spectrograms. Models of RPA curves (radial and axial heads) and spin curves (radial head only) are available which, when fit to specific data, yield the density, temperature, flow velocity, spacecraft potential, and heat flux. However, this procedure is applicable only to the low mass channel data, where the energy response width exceeds the 50 V retarding potential sweep range. It is provisionally applicable to He+ in the high mass channel ($\triangle E/E$ FWHM = 51 eV), though care should be exercised in dealing with warm or high-speed He+. For very warm (> few eV) or heavy ion plasmas or for plasmas exhibiting highly non-Maxwellian features (multiple or highly asymmetric spin curves, or multiple RPA "knees"), other techniques are more useful in deriving quantitative information.

An alternative to the curve fitting procedures is the generation of distribution function values, with subsequent integration of appropriate moments to derive bulk parameters. This procedure is limited to the period before the radial RPA failure for light ions viewed with the low mass channel, but can be used for the high mass channel data throughout the life of RIMS due to the differential response of that channel. It should be noted that the light ion data are processed by the differentiation technique, which magnifies statistical noise present in the data. The heavy ion data are directly interpreted as differential intensity, with appropriate adjustments for the presence or lack of RPA potential. A full matrix inversion deconvolution technique has been tested but not implemented.

When RPA data are unavailable for the light ions so that full distribution functions cannot be produced, it is possible to directly infer bulk properties such as density and flow velocity by working with radial detector spin curves, interpreting them as first velocity moments (flux) of the distribution function in each look direction. The spin curve centroid gives the direction of flow. The geometry of the spacecraft motion relative to the magnetic field, in conjunction with local electric field measurements of the plasma transverse motion, yields the total velocity vector in the spin plane. Dividing the integral flux by the total velocity yields the ion density while the spin curve width provides an estimate of the temperature. The results of this procedure have been demonstrated to be consistent with results obtained by a fitting procedure based upon the spin curves.

Access to the full RIMS data may be obtained by running the program ENSP3D (user documentation is available separately). Output from ENSP3D is in the form of flux versus retarding potential, flux versus spin phase angle, or flux, intensity, or phase space density versus both energy and spin phase angle. RPA and spin curve files may be created and subsequently fit using one or more of the available models. Distribution function files may be used as desired for integration or further analysis. A variety of plot formats is accessible through ENSP3D.

III. ABSOLUTE IN-FLIGHT CALIBRATION

A. Cross Calibration Between RIMS Electrometer/Channeltrons

The total current electrometer present in the RIMS aperture provides for an intercalibration with the mass spectrometer that yields a continuous measure of the absolute response of the channeltrons and the effective area of the spectrometer. This cross calibration is best carried out at low altitudes where the electrometer signal is strong. Unfortunately, the channeltron count rates are then close to saturation, an effect which must be compensated for to produce meaningful calibration numbers.

This calibration provides a measure of the product of the effective entrance aperture area and the detection efficiency of each channeltron. The resulting numbers have units of [cm^2] and will be referred to as AEPSL and AEPSH, referring to the low and high mass channels, respectively. In this process, it is necessary to properly account for the head, channel, mass, and energy-dependent solid angle response of RIMS. It is also necessary to compare the response of the high and low mass channels to the same ion species (generally He+), and to compare the sum of all major ion species responses with appropriate integration over solid angle to the electrometer current. The calibration may be repeated on an orbit by orbit basis, or even a minute-by-minute basis when good electrometer data exist, providing ongoing correction for channeltron degradation during the course of the mission.

A program has been developed for automating the calibration procedure, known as RIMCAL. Having chosen an appropriate data interval from the summary fiche and having established the data set as a disk file, the user is prompted for a description of the data location. RIMCAL then provides plots of spin curves of the electrometer and the major ion species. The user inspects these plots and develops estimates of the saturation count rates for the low and high mass channels. RIMCAL is then run again in a calibration mode under which the user is prompted for the saturation count rates, corrections to the raw data are made, and new plots of the corrected data are provided. The major criterion for successful correction is that the He+ curves from the high and low mass channel should have identical shapes (though not necessarily identical count rate maxima). RIMCAL also provides plots of the correction curves used (which are based upon a model to be described below), a summary file of the fluxes of each ion species, and the derived calibration values. The results are stored by updating a file which is consulted by other RIMS software when converting count rates to physical parameters.

The data period of day 314, 1981, 1025 to 1031 UT was selected for an initial demonstration of this procedure. The results are summarized in Figures 9a, b, and c. Figure 9a shows the spin curves of the electrometer and the two major ion species H+ and O+. Figure 9b shows the high and low mass channel He+ response. In each case, the dashed curve is the raw count rate, while the solid curve represents the response after correction for saturation. The resulting values of AEPSL and AEPSH are shown in panel B. For consistency, it is required that the corrected He+ curves have essentially the same shape. Figure 9c shows the saturation correction curves used to correct the data. Note that the low mass channel has a somewhat lower response than the high mass channel at this time, presumably due to channeltron gain degradation. This is corroborated by the fact that the low mass channel is saturating at a lower rate than the high channel. It should be noted that these derived calibration values must be used in conjunction with the laboratory

measured energy-dependent solid angle aperture appropriate to each channel and ion species. These solid angle values are available through the subroutine CALCON.

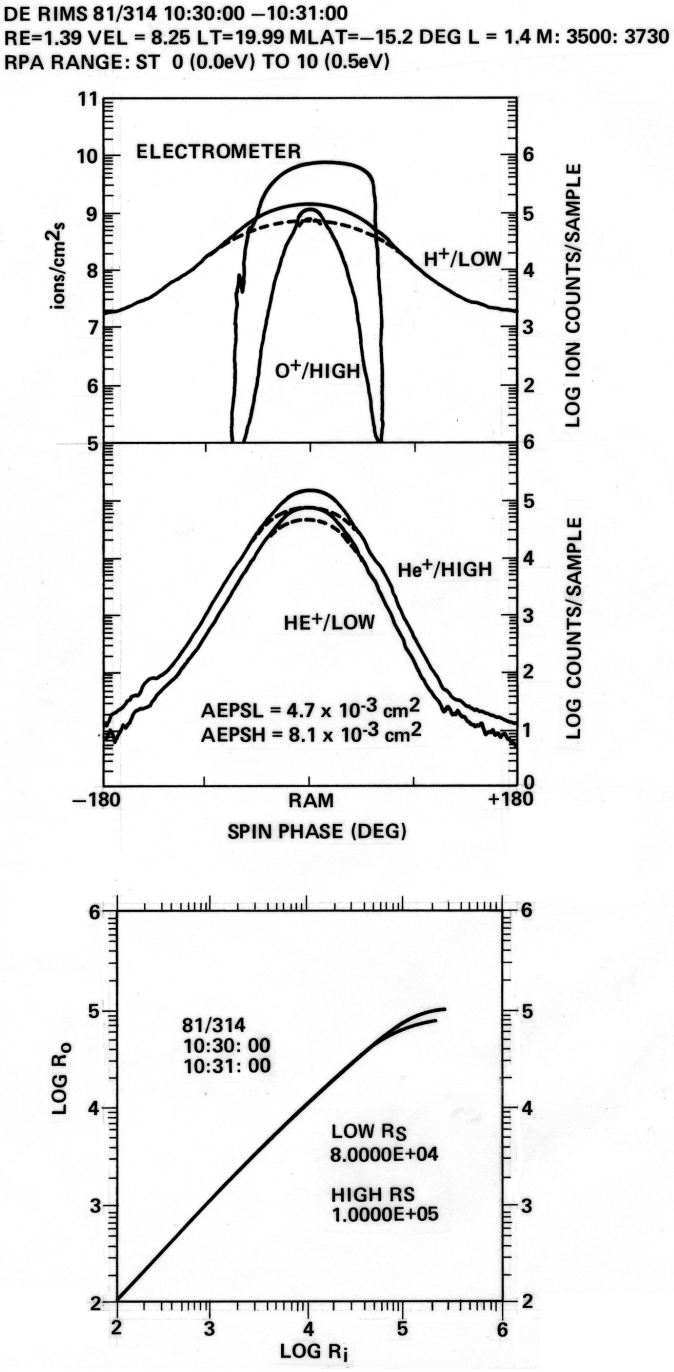

Figure 9. Calibration summary for day 314 of 1981. (a) spin curves, H+, O+, electrometer. (b) Spin curves He+. (c) Saturation curves.

B. Correlation with PWI Density Measurements

The Plasma Wave Instrument (PWI) on DE 1 routinely provides a measure of the plasma electron density through determination of the upper hybrid resonance frequency. The range of densities which can be measured this way extends from approximately 10 cm^{-3} to 104 cm^{-3}, limiting this technique to regions within the plasma-sphere. Using a Maxwellian fitting procedure, it has been determined that the densities determined from the RIMS count rates are in good agreement with those derived from the PWI measurements when the AEPS factor is taken to be 4.4 x 10^{-3}. Figure 10 shows RIMS and PWI densities for a partial orbit. Good agreement is found throughout the plasmasphere. Disagreement after 1245 UT is attributed to spacecraft potential induced errors. This provides a reassuring corroboration of the self-calibration of the RIMS sensor.

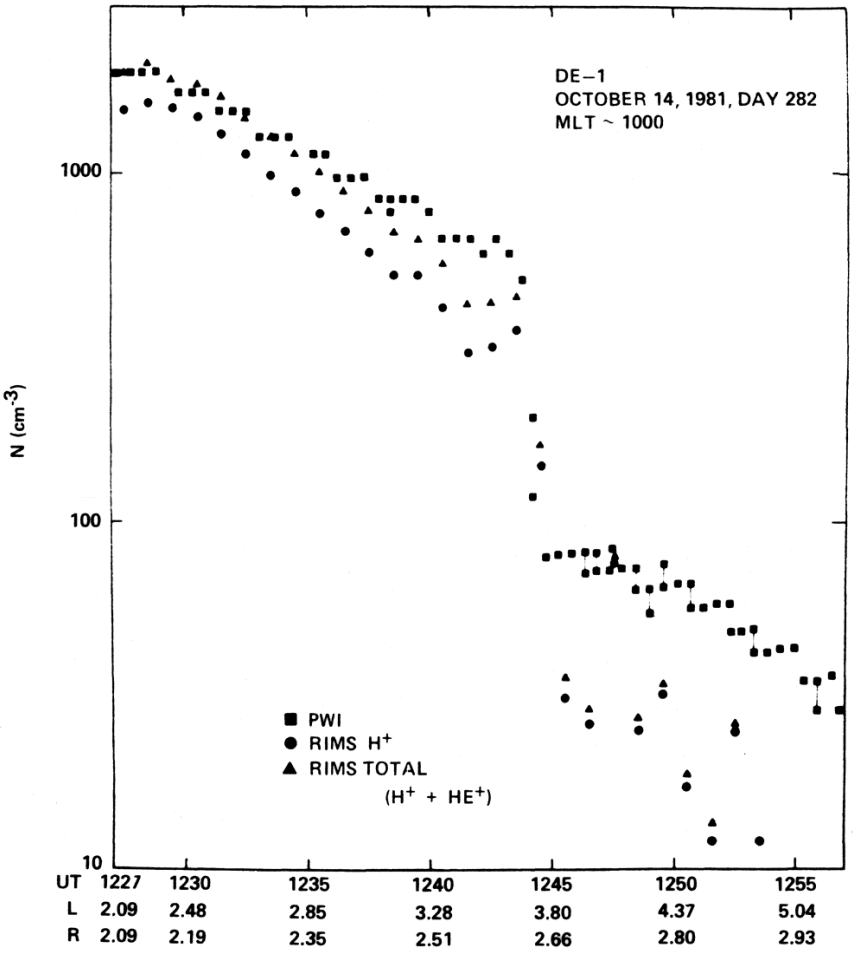

Figure 10. Comparison of RIMS ion density measurements and electron densities derived from the DE 1 Plasma Wave Instrument.

C. Channeltron Saturation Model

The channeltron saturation noted above is a well-known effect in such systems. A model of the effect for the RIMS instrument has been developed to facilitate correction for saturation effects during analysis.

1. System model. The system model is shown in Figure 11. The channeltron output is fed into a charge-sensitive preamplifier (CSA). The relationship between the preamplifier voltage output and the input charge pulse is given by:

$$V_{OUT} = G\, e/C_f\,, \tag{24}$$

where G is the chaneltron gain for a pulse, e is the electron charge, and C_f is the CSA feedback capacitance. The voltage pulse V_{OUT} is subject to a threshold discriminator with threshold V_T such that for $V_{OUT} < V_T$, no output results and for $V_{OUT} \geq V_T$, an output pulse is produced. The discriminator output is assumed to be a pulse with fixed width and amplitude, and this pulse is in turn fed to counter circuitry.

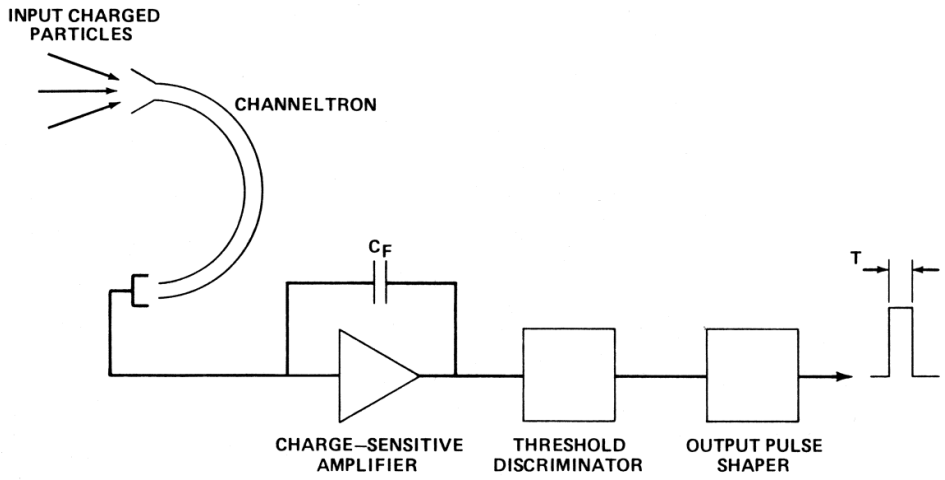

Figure 11. Functional representation of the RIMS detector pulse shaping electronics.

Figure 12 shows a model of pulse height distribution and threshold discriminator level that contributes to the saturation effect. At low count rates, essentially all of the pulses are above the discriminator level and there is no loss. As the input count rate R increases, the average gain decreases, meaning that the pulse height distribution shifts to the left and also may change shape, with more and more pulses falling below the discriminator level. Hence, the observed count rate decreases. In the extreme case, the average gain is reduced to the point where essentially all of the pulses fall below the discriminator level and the output pulse rate falls to zero.

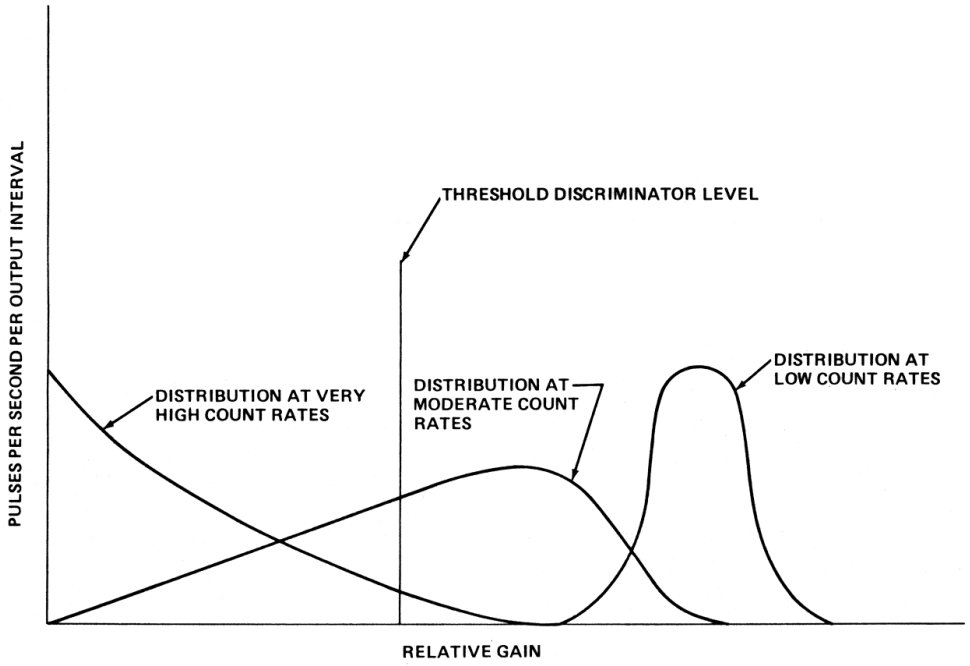

Figure 12. Schematic dependence of channel flow pulse height distribution on total count rate.

2. Definitions.

R = true count rate of channeltron, defined as the number of input particles /second to the channeltron

r = observed count rate, i.e., rate of logic pulses output

$G_o(R)$ = count-rate dependent mean channeltron gain

G = equivalent gain for a single pulse

V_t = threshold discriminator setting ($V_t = eG_t / C_f$)

n = count rate observed at output of threshold discriminator

dn(G) /dG = pulse height distribution probability function, the number of pulses per second resulting from gains between G and G + dG.

3. Output pulse height distribution. The normal output pulse height distribution is modeled as a Gaussian distribution of the form :

$$\frac{dn(G)}{dG} = \frac{R}{\sqrt{2\pi}\,G} \exp\left[\frac{-1}{2}\left(\frac{G-G_o(R)}{G}\right)^2\right] \tag{25}$$

At very high rates or when channeltrons are degraded, the distribution will lose its well-defined peak and assume an exponential form:

$$\frac{dn(G)}{dG} = R \exp\left[-\frac{G}{G_o(R)}\right] \tag{26}$$

The effective counting rate is given by :

$$n = dG \int_o^\infty \frac{dn}{dG} \qquad \text{and} \qquad G_t = V_t C_f \tag{27}$$

The behavior of chaneltron pulse height distributions is not well documented as a function of R, but it is known that a gradual transition occurs from the Gaussian to the exponential forms above.

4. Model of $G_o(R)$ as a function of R. Galileo Electro-Optics Corporation data sheet 4000B, dated September 1980, gives data on the gain of 4800 series channeltrons as a function of count rate and output pulse height distributions. For the curve given, at count rates greater than 106/sec, the curve approaches an inverse relationship to R. This can be understood in terms of a limit on the current which the channeltron can provide in the form of output pulses,

$$e\ R\ G_o(R) = I_{max} = \text{constant as } R \to \infty \tag{28}$$

5. Computation of effective counting rate n. Adopting the exponential pulse height distribution to describe the saturation effect, we have from (26) and (27)

$$n = R \exp[-G_t/G_0(R)] \quad . \tag{29}$$

Defining $R_s = I_{max}/e/G_t$, equations (28) and (29) give:

$$n = R \exp[-R/R_s] \tag{30}$$

A sample of this relationship is plotted in Figure 13 for Rs = 7 x 106 Hz (see also Figure 9c).

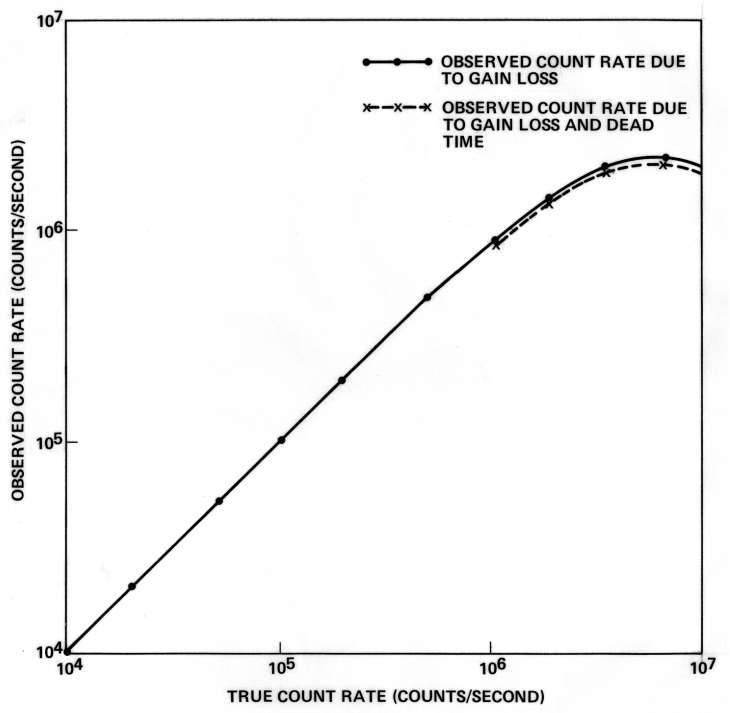

Figure 13. Saturation model for Rs = 7 x 106 Hz, T = 50 ns.

6. Effect of dead time. The preamp/discriminators produce pulses of a constant and non-zero width. Let this pulse width be T. If two pulses arrive within this interval T, then one pulse will be lost. The loss due to dead time can be estimated by a probability calculation based on the assumption that the temporal distribution is Poissonian. The result, given in Fillius [10] is:

$$r = n \exp[-nT] \tag{31}$$

The observed counting rate r is due to a combination of two effects, the first being the gain loss at high counting rates and the second being the dead time correction. Which effect is the most important is dependent upon the value of the dead time, the functional dependence of the gain upon input counting rate, and the value of the threshold discriminator level. Combining equations (30) and (31) gives :

$$r = R \exp[-R/R_s] \exp[-RT \exp(-R/R_s)] \tag{32}$$

The RIMS preamplifier electronics and counters have been designed with a pulse width of <50 ns, so that dead time effects are not important below 10 MHz. Since saturation is observed at lower rates, it is clear that channeltron gain degradation is the controlling factor. Hence, we have adopted the simple model of equation (30) for use in correcting RIMS data, where R_s is determined empirically by examining obviously saturated data.

7. Conclusions. The model presented above reproduces the essential features of the effects seen in the RIMS data, namely, the double-valued response of the counting rate as the RPA voltage is increased and the temporal decrease in the channeltron "efficiency," the latter actually being due to a temporal decrease in the channeltron gain. This effect can actually be rather

insidious, for if the average pulse height is not very far above the threshold level, the degradation and partial recovery of the channeltron with exposure to high counting rates and/or contamination will result in erratic changes in the calibration.

Future instrument programs should include saturation documentation of the channeltron amplifier-discriminator-pulse shaper combination. A point radioactive source can be used at variable distances from the channeltron to produce a known input count rate. Alternatively, the ion gun in conjunction with pinhole apertures in front of the channeltron can produce known input counting rates. The most significant unknown in the system is, of course, the rate-dependent pulse height distribution form, which may also be a function of time as the channeltrons degrade with accumulated counts.

Ideally, RIMS-type instruments would be designed in such a way as to be protected from saturation by means of mechanical or electrical variable apertures, thus increasing the useful dynamic range of the data.

IV. ANOMALIES IN RIMS OPERATION

A. Introduction

The Retarding Ion Mass Spectrometer (RIMS) on Dynamics Explorer 1 (DE 1) was designed to perform energy and mass analysis from 0 to 50 eV on ions ranging from mass 1 to 40 amu. This requires extremely fine control of the potentials and fields near and within the instrument, particularly at the lowest energies, i.e., less than 2 eV. Shortly after the launch of DE 1, it became clear that RIMS was not behaving exactly as planned, and that there were a number of potential problems. After several months in orbit, further anomalies occurred, changing the operating characteristics of the instrument. The purpose of this section is to catalog these anomalies, describe the nature of the illustrative data, suggest mechanisms for the failure modes, and propose methods for dealing with these problems when analyzing the data. Six anomalies have been recognized in the RIMS data:

1) Calibration of the instrument channeltron with respect to the electrometer and the upper hybrid resonance observations of the Plasma Wave Instrument (PWI) shows that the RIMS geometric factor is about a factor of 5 lower than laboratory calibrations. There is, contrarily, an apparent increase in efficiency at retarding potentials below 1 V, primarily affecting cold plasma measurements in the end heads.

2) There is spin modulation to the end head data that is primarily noticed in the "ionospheric" measurements, i.e., in cold dense plasmas where the flow past the head is at high Mach numbers.

3) Beginning at launch, it appeared that the +Z, or number 2 head, was biased by -2 V with respect to the other two heads. On day 73 or 74 of 1982, the -2 V anomaly disappeared from the +Z head.

4) The floating potentials of the three sensors appear to differ by a few tenths of a volt. This is most apparent at eclipse transitions, where the sensor potentials shift by different voltages.

5) On November 25, 1981 (day 329), the radial detector retarding potential failed. The two end heads were unaffected. The radial detector retarding voltage occasionally becomes effective again, most notably on days 45 and 46 of 1982.

6) At some time during the 1981-82 winter, the aperture bias feature of the -Z Head (head 3) was apparently shorted out. It is not working properly as of day 45 of 1982.

B. Detector Efficiency

The detector calibration efforts involving flight data were discussed earlier in this report. These comparisons established that the RIMS flight effective area was about 20 percent of the value determined by pre-flight calibration. At retarding potentials below 1 V, a different effect becomes apparent, primarily in the -Z head: an increase in the detector efficiency of a factor of 5 to 10 with respect to the higher energy response. This is illustrated in Figures 14, 15, and 16, which show distribution function and RPA plots from the -Z and radial detectors. The distribution function technique emphasizes the nature of the problem, while analysis of RPA curves will tend to mask it. The effect is independent of spacecraft potential, indicating that this is an internal instrument effect, and not a sheath effect. Figure 14 shows the radial detector, ram data converted to phase space density. The rammed plasma is well modeled to below 1 eV, indicating that the detector response below 1 V (RPA) is consistent with the higher energy response of the detector. The deconvolution of the RPA curve, and subsequent fit, do not take satellite sheath effects into account, and modest variations are found from the more sophisticated analysis technique developed by Comfort, et al. [8].

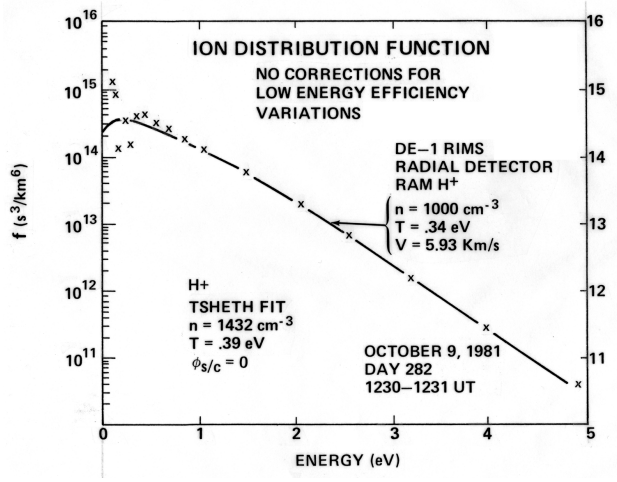

Figure 14. Comparison of derived phase space density and a Maxwellian fit.

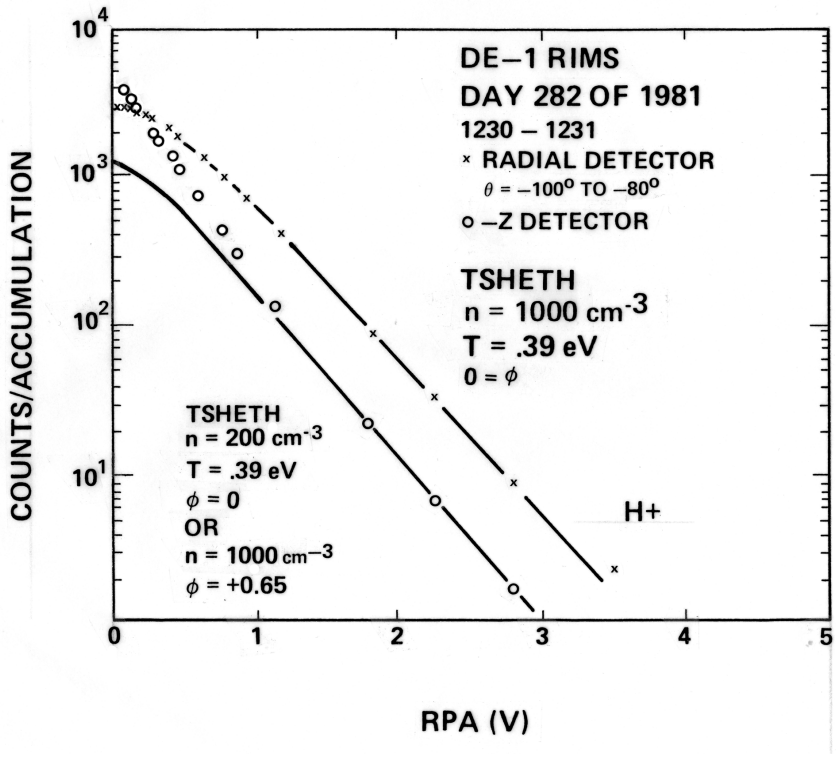

Figure 15. Comparison of raw data and Maxwellian fits.

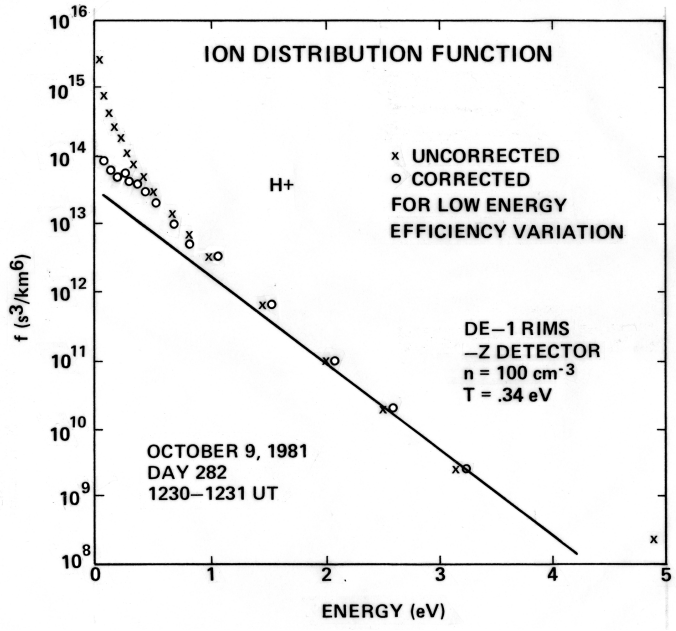

Figure 16. Comparison of derived phase space densities and Maxwellian fits.

Figure 15 shows radial head (at 90 deg spin phase) and end heat data in raw form, with fits using Comfort's sheath program, based on analysis of the ram data from the radial detector. The end head data agree if the -Z detector is +1 V with respect to the satellite and the ambient plasma, in the 1 to 3 V RPA range. It can be seen that the -Z data rise above the predicted response below 1 eV. Once converted to distribution function form, the problem is even more apparent (Fig. 16). The deviation from the fit is apparently independent of sheath effects, since this behavior is largely unaffected by satellite potential changes at eclipse transitions. It is therefore inferred that this is an instrumental effect. The gap between the observed 0-1 eV data and the model was modeled with short exponential segments, and the calculated distribution function was then corrected to fit the model curve. The one set of correction factors has proven adequate over a wide range of plasma environments. Figure 16 shows the corrected distribution function.

1. History. The low energy efficiency variation shows no known time variations.

2. Probable mechanism. The overall reduction of the throughput in comparison to the ground calibration does not have an obvious cause. However, the fact that the radial electrometer data agree with the PWI results indicates that this is not a sheath effect, since the flux into the instrument passes through sheaths which vary tremendously over the RIMS measurement range. Hence, the reduction in counting rates occurs somewhere between the electrometer collector and the channeltron. This part of the instrument should be insensitive to the usual questions that can be raised about laboratory testing. A possible, though not very convincing answer, is that the channeltrons of all three heads were approximately equally contaminated during transport, or during installation in the spacecraft. No other plausible environmental changes, such as stray magnetic fields, etc., have been found which can account for the nearly identical changes in the three heads.

The laboratory calibration may be questioned. Due to the constraints of launch deadlines, some anomalous results were obtained, such as fluctuation in the counting efficiency at different count rates. If the PWI data is taken as correct, then the loss rate in the Ion Mass Spectrometer (IMS) is about 80 percent, which, while lower than desired, is not an unreasonable efficiency for such a complicated instrument.

The increase in count rates at very low energies, <1 eV, is contrary to normal instrument behavior. A very likely solution may be found by noting that the electrometer collector plate has a hole in it, as opposed to a grid, to allow ions to reach the IMS without loss. This also decreases the uncertainty in the electrometer collector area. This hole is a circle for the Z heads, and a rectangular slot for the radial head. The collector plate is held at the aperture plane potential, and has before and after it 90 percent transparent conducting grids which are both biased -10 V with respect to it. This configuration, shown in Figure 17 [11], forms a strong converging lens for very low-energy particles. Since the focal length of the lens increases with increasing energy, the lens becomes progressively less efficient at focusing particles off-axis. The observed behavior of the data is in qualitative agreement with this, and approximate corrections are easily made. The exact corrections will be functions of the Mach number, the input apertures of the instrument, and any plasma flow. A detailed system simulation of the complete optics is beyond the range of this study, but should be undertaken during the design phase of future instruments so that such effects can be anticipated.

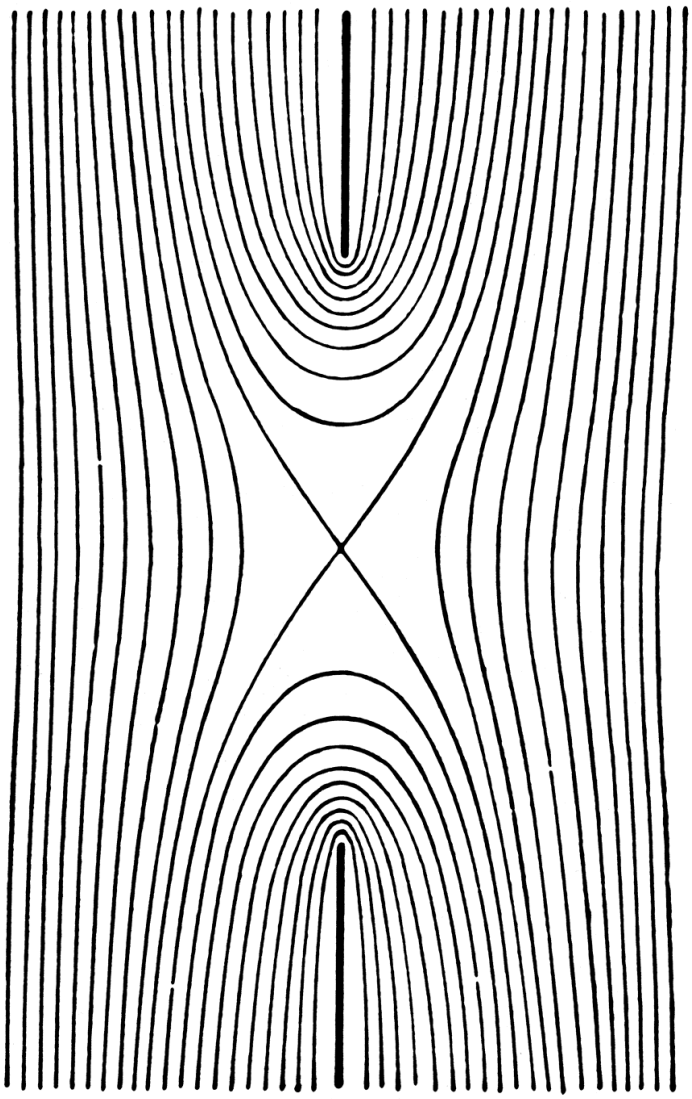

Figure 17. Aperture midway between plates at the same potential.

C. End Head Spin Modulation

The end head apertures were supposed to be symmetrical about the spin axis, and should not demonstrate response variations with spacecraft spin. They do show spin variations, however, primarily at low altitudes, in cold, dense plasmas at high satellite velocities (i.e., mostly in the ionosphere). Figure 18 shows spin curves from the end heads illustrating this effect. The spin modulation increases with mass; i.e., there is a modest variation in the H+ flux and a large variation in the O+ count rate.

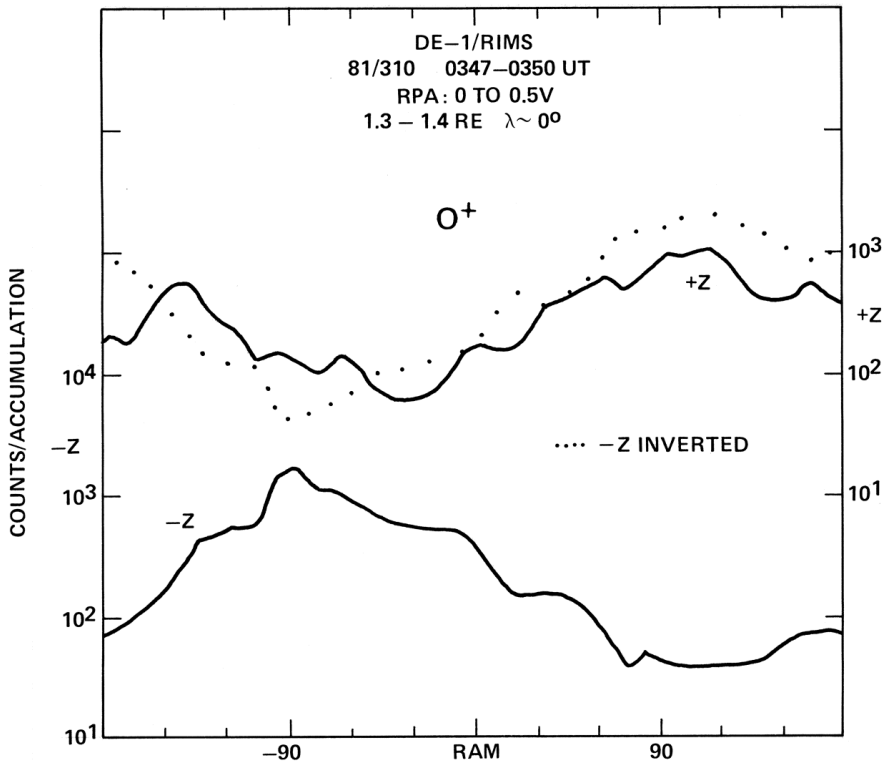

Figure 18. Example of spin modulation of axial head count rates.

1. History. This effect appears to be constant.

2. Probable mechanism. It was initially felt that this might be a charging effect, since the LIMS and UCSD experiments on SCATHA revealed a 1 V spin modulation of the spacecraft potential. Such affects were considered for DE 1, but the phases of the +Z and -Z spin modulations are nearly 180 deg apart (as seen in Figure 18), not in phase as they should be for an oscillation in the spacecraft potential. Continued analysis of the end head data suggested that the RIMS detector assemblies were not as completely grounded as had been supposed, and that they were not necessarily tied to the same potentials. Comparison of the RPA curves for O+ taken at different spin phases for the -Z head are consistent with a 1-V modulation in the detector potential. The +Z head data are less clear, since the -2 V anomaly (described below) makes interpretation of those RPA curves difficult. The problem with this interpretation remains the lower modulation of the H+ and He+ fluxes, which suggests this is not simply a potential modulation.

There is a method for obtaining a preferred direction for the RIMS detectors, based on the internal instrument geometry. Since the Z heads are not exactly on the spin axis, arriving particles are more affected by the spacecraft potential when they arrive from one direction than the other with respect to the spacecraft frame of reference, thus compounding the variation. Other physical processes which might be at work include wake asymmetries, particularly on the +Z axis due to the S-band antenna.

3. Solution. High Mach number flows past the ends of the satellite are not well understood, though the modeling of such flows using the CRAY computer done for the radial detector spin curves could be extended to include Z head measurements. Choosing data with the radial head always in the same phase with respect to the ram velocity will allow comparisons between the end heads, though caution must be used.

4. Impact on science. None, if the above precautions are taken.

D. Two-Volt Anomaly

When the first RIMS data arrived, it immediately became clear that there was an apparent 2-V difference in the end head potentials. Figure 19 illustrates this effect. The RPA curves (adjusted for geometric factor differences) appear nearly identical, except for the 2-V shift. Closer examination shows a lower slope on the +Z (-2 V) head curve, suggesting a higher temperature at that end. This effect persists in all environments, and appears to have been independent of environmental effects. Comparison of the zero volt aperture bias data with the aperture bias sequence of day 287 of 1981 shows that the appearance of the data is as if there were a -2 V aperture bias imposed on the detector at all times, with an additional -2 V added to any intentional bias voltages.

1. History. The 2-V anomaly does not appear in the data set taken on day 74 of 1982, beginning at 02:00 during ascent from perigee. During this time RIMS was being cycled through an aperture bias sequence. The 2-V anomaly does not reappear in any data taken after this. It is not clear if the difference in slope continues past this time.

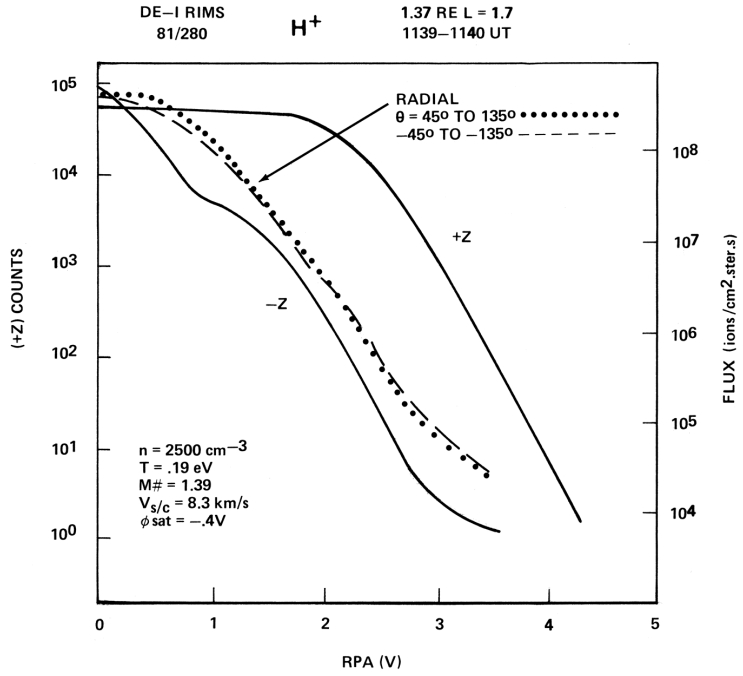

Figure 19. Example of comparison of RPA curves from the radial and axial heads.

2. Probable mechanism. A greatly simplified schematic (Fig. 20) shows how the bias voltages are supplied for all three RIMS heads. Only one relevant component is shown. The aperture plane bias, V_a, the retarding potential, V_r, and the offset -10 V supply with respect to V_a are power supplies for all three heads. Voltage sources are shown as batteries which replace entire circuit boards, and small resistors are ignored. The 100 k ohm isolation resistors provide for electrical failures resulting in contacts to other system components. In theory, they should completely isolate the other two heads. The physical location for the resistors for the retarding potential are in the central power supply, while those for the aperture plane bias are located in the individual heads. We assume a mechanism that must affect only one head, and so postulate a spurious resistance, R11. This forms a simple voltage divider circuit, requiring that at zero retarding potential the offset voltage between V_a and point A is -2 V. Setting R_{11} to be 500 k ohms, the voltage actually delivered to the retarding grid V_{rp}, referenced to the aperture plane, is given by the equation:

$$Vrp = 0.83\ Vr - 2.0 \qquad (33)$$

This results in a voltage shift which is approximately independent of Vr, and will cause the temperature of the distribution derived from the +Z head to be somewhat higher than the true value. Since only the retarding power supply voltage is telemetered, not the voltage actually delivered to the instrument head, the count rate will seem to change more slowly with respect to the retarding potential than is the a actual case. Such a bridging resistor would be a bit of grit, thermal insulation, or similar matter lodged in the head during construction or installation. It could easily remove itself due to thermal effects or mechanical vibration transmitted from other parts of the spacecraft. This grit must be a poor conductor, and once free, is unlikely to force itself back into a shorting position, or to be welded there by surge currents. Joule heating to clear the short from the current flow is a distant possibility to remove the bridging matter. While the exact moment of change is not known, after day 74, the data from the +Z head appear normal.

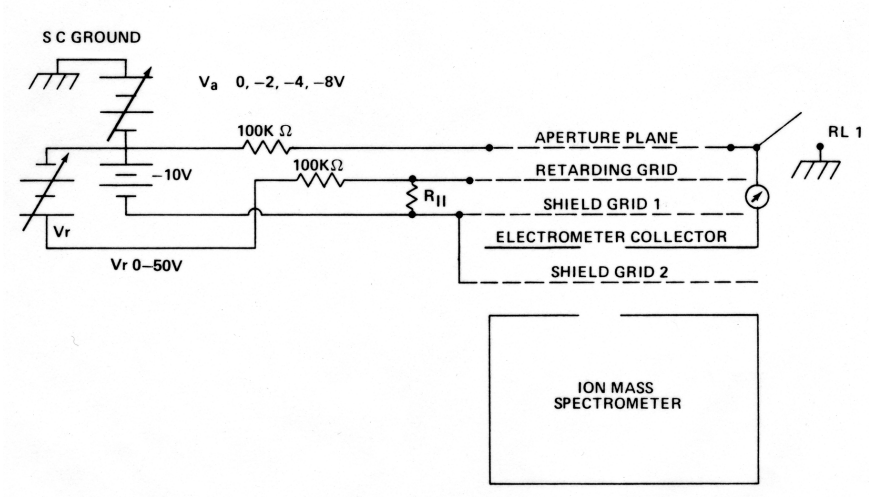

Figure 20. Schematic diagram of RPA and aperture biasing of the RIMS sensor heads.

1. Solution. Prior to day 74 of 1982, the voltages must be corrected according to the formula : Vrp = 0.83 Vr - 2.0.

2. Impact on science. The 2-V anomaly effectively prevents flow velocity measurements prior to day 74 of 1982. Unfortunately, the early instrument modes leave very little energy resolution in the 2 to 5 V range, so there is little or no resolution of the plasma energy distribution. Automatic analysis of distribution functions (in particular the numerical integration routine) fails when the plasma temperature is less than the 2-V offset, i.e., in the plasmasphere.

E. Detector Assembly Potential Differences

Analysis of the spring 1982 eclipse data for density and temperature also produced a set of measurements of the shift in spacecraft potential at the eclipse transitions. The detector assemblies consistently shifted potential by 0.4 to 1.0 V when the ambient plasma was in the 50 to 500 cm^{-3} density range. Although the absolute potential was difficult, if not impossible to obtain for the end heads, the combination of sunlight and eclipse data allowed unique determination of the radial detector potential from the spin curve. Unfortunately, the three assemblies did not shift by the same amount, indicating that the floating potentials of the detectors varied from one another. Assuming a reasonably isotropic environment in eclipse, it seems likely that the detectors were closer to equal potentials in eclipse than sunlight, where photoemission provides a large asymmetry. It appears, therefore, that the change in net current of the RIMS detector assemblies through the aperture planes was biasing the heads by differing potentials.

This effect would be most obvious when one end is facing the Sun, i.e., when the spin axis is along the Earth-Sun line. This was the case early in the satellite lifetime. An example is day 81/317 at 0650 UT. In spite of an ambient plasma density over 1000 cm^{-3}, the -Z detector, which is toward the Sun, is 0.2 to 0.3 V positive.

1. History. This phenomenon should vary with season.

2. Probable mechanism. The three instrument heads are fed from common power supplies (Fig. 21) in the central electronics assembly (see Section IV.D). To insure that individual head failures would not cause complete system failure, 100,000 ohm isolation resistors were used in the key supply leads to each head. While a simple and effective system that has already proved its worth in the radial head failure, this system allows for some slight uncertainties in the potentials of the heads. This uncertainty is not only between the individual heads, but in the grid potentials within the heads. The primary sources of these shifts should be the photoelectrons being emitted from the conductors in the head. A 1 μA current through the isolating resistors would result in a 0.1-V potential shift. This would not be telemetered, since the voltage telemetered is that of the power supply, but must be inferred from shifts in the data during times of eclipse. Clearly there is the potential for shifts between the end heads due to different exposures from the Sun. Additionally, small spin modulations during the spin of the spacecraft should be expected on the end heads, with somewhat larger variations seen in the radial head. The magnitude of these variations may be on the order of a volt, but usually will be less. Exact predictions cannot be made, since the magnitude of the current depends critically on the spacecraft orientation.

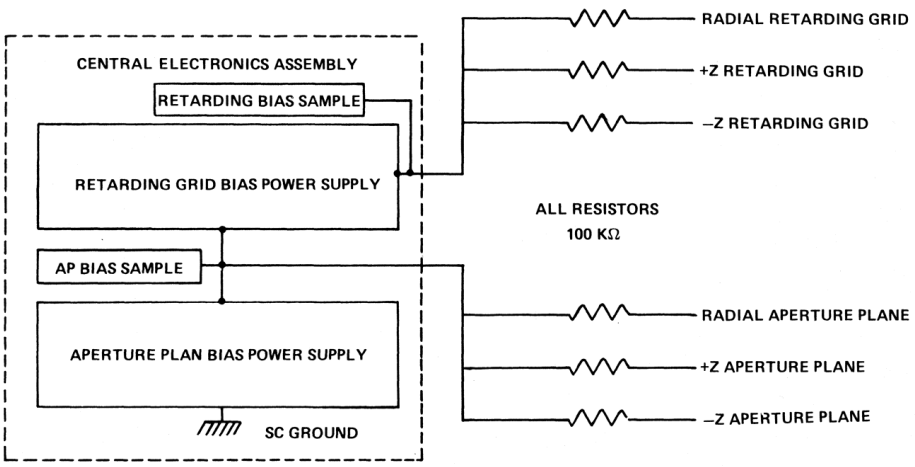

Figure 21. Functional diagram of RIMS aperture and RPA biasing electronics.

3. Solution. The exact potential of the head in question must be determined by examination of data from that head.

4. Impact on science. The effect is of no importance for plasmas that have few particles near the spacecraft potential due to ram, flow, or temperature effects. Individual determinations for each head will need to be made when the above conditions are violated.

F. Radial RPA Failure

At 19:50 UT on November 25, 1981 (day 329), the radial detector retarding potential failed to operate properly. Little or no retarding action was found, though the other heads continued to operate normally. The hydrogen and helium data for this time are shown in Figure 22. The change is particularly clear in the He+ data (bottom panel).

1. History. The initial failure occurred on day 329 of 1981, beginning 30 min after the activation of the instrument for that orbit. The retarding potential has occasionally come back to life. Known periods where the retarding potential appears normal are:

82/045	20:00	to	82/046	04:00
82/046	05:15	to	82/046	06:15

2. Probable mechanism. The most plausible reason for this failure is that the radial retarding grid is shorted to either the adjacent shield grids or to the instrument ground. As discussed in the following power supply section, the instrument uses a single power supply in the central electronics assembly for all three retarding grids. Each line is isolated by a 100 K ohm resistor, so that a failure at an individual head will not normally effect the other heads.

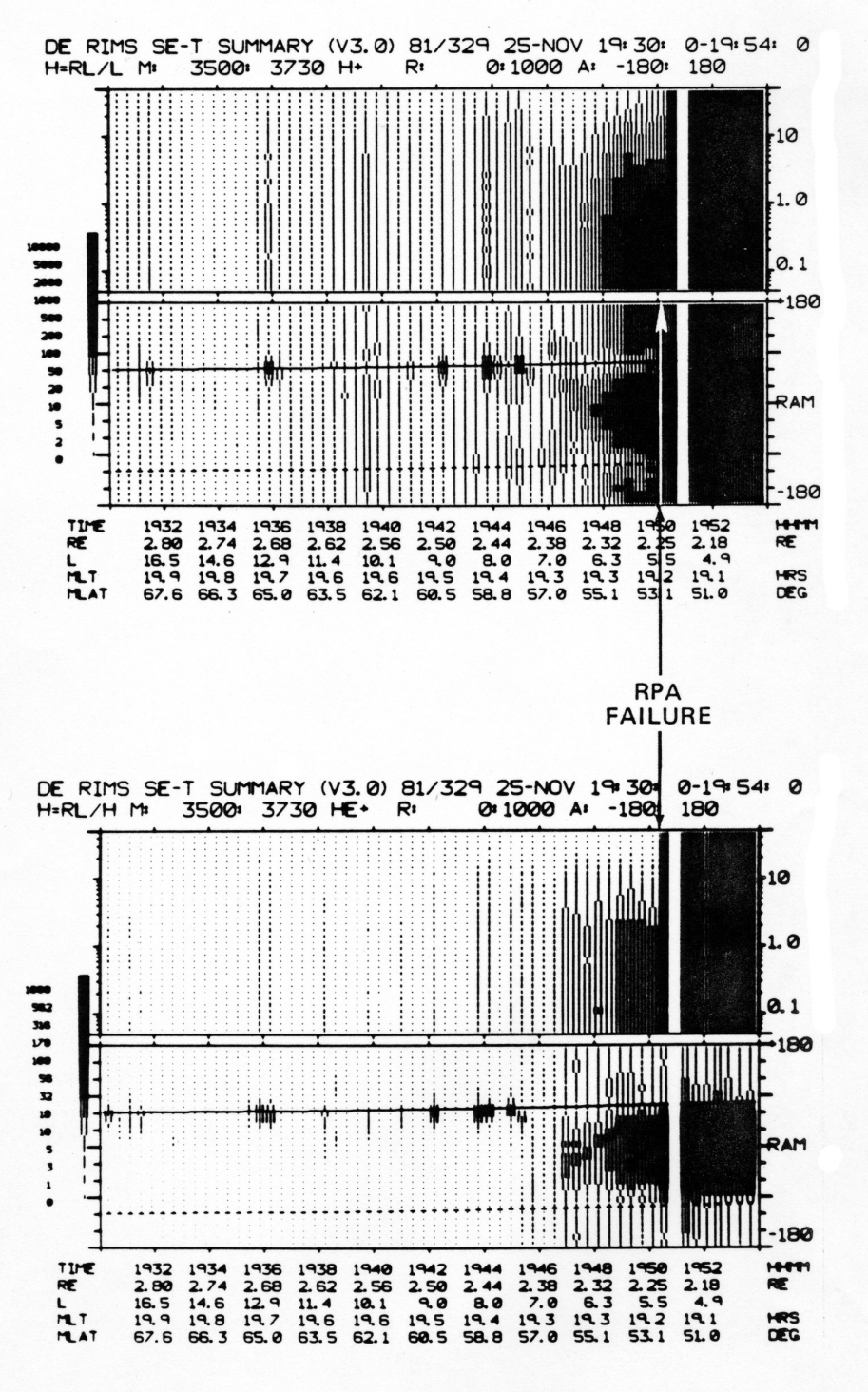

Figure 22. Retarding potential and spin spectrograms for H+ and He+ showing the failure of the radial head RPA sweep.

The most likely agent is a bit of metal trapped between either the grids during assembly or within some other section of the instrument where the retarding potential is available. Ultraviolet

radiation, charged particle impacts, and prolonged outgassing insure that all internal surfaces lack the normal layers of protective adsorbed gases found on even the cleanest terrestrial materials. In microgravity, foreign matter would drift until chance brought it into contact with the retarding potential and a conductor at another potential. While isolating resistors limit steady current, even a very small surge current represented by the capacitance of the grids could effectively weld the bit of grit into place. Once in place, it ordinarily would stay there until some thermal or mechanical stress broke it loose. The stable location would in fact be the shorted one, since attachment can always occur, while detachment requires more specialized conditions. This scenario is supported by the fact that the resumption of the operation of the retarding grid occurred on day 45 of 1982, just after the spacecraft had passed through eclipse, and had been subjected to considerable thermal stress. Shortly thereafter, the failure resumed, perhaps during eclipse exit at 06:18 on day 46 of 1982.

3. Solution. Use the spin curves for temperature analysis, or the end heads where possible. Total counts will be accurate, since the effect is as if the retarding voltage was constantly zero. The sweep of the mass analyzer voltage, designed to complement the retarding voltage, provides some energy analysis for the high masses (nitrogen and oxygen) due to the differential nature of the mass spectrometer and the relatively narrow energy acceptance window for those ions.

4. Impact on science. To the extent that isotropic plasmas can still be analyzed using the end head RPAs and the spin curves from the radial detector, the radial detector RPA failure can be compensated for. The main problem is in anisotropic plasmas, where the characteristics of field-aligned plasmas can no longer be determined.

G. Aperture Plane Bias Failure

During the winter of 1981-82, the aperture plane bias capability of the -Z head was lost. Figures 23 and 24 show the characteristic RPA curves, showing the normal behavior in the +Z detector (Fig. 23) and the' lack of increase in count rate expected in the -Z detector (Fig. 24).

1. History. No changes have been noted since the initial failure.

2. Probable mechanism. A key point to note is that the retarding supply is biased with respect to the aperture plane supply from a reference point within the power supply. The RIMS schematics show a direct connection for the retarding volt-age to the appropriate grids, with no connections between the isolation resistors and the grid. This implies that any change in the retarding potential or aperture plane power supplies should be visible on all three heads. Alternatively, single head malfunctions imply that spurious connections occur within the head itself. Possible malfunctions would include a bridging of adjacent grids or paths to the spacecraft or instrument ground, with foreign objects. This could result in a hard short, but could equally well result in a high impedance circuit with subtle effects on the instrument response. The failure of the bias is almost certainly due to the failure of relay RL 1 (Fig. 20), or, less likely, an arc caused by differential charging has tracked the insulator separating the aperture plane from the spacecraft ground. Under either condition, the result would be that the applied retarding voltage would be offset by the aperture plane bias, since the retarding potential is referenced at the power supply, while the aperture plane would be locked at or near the spacecraft ground.

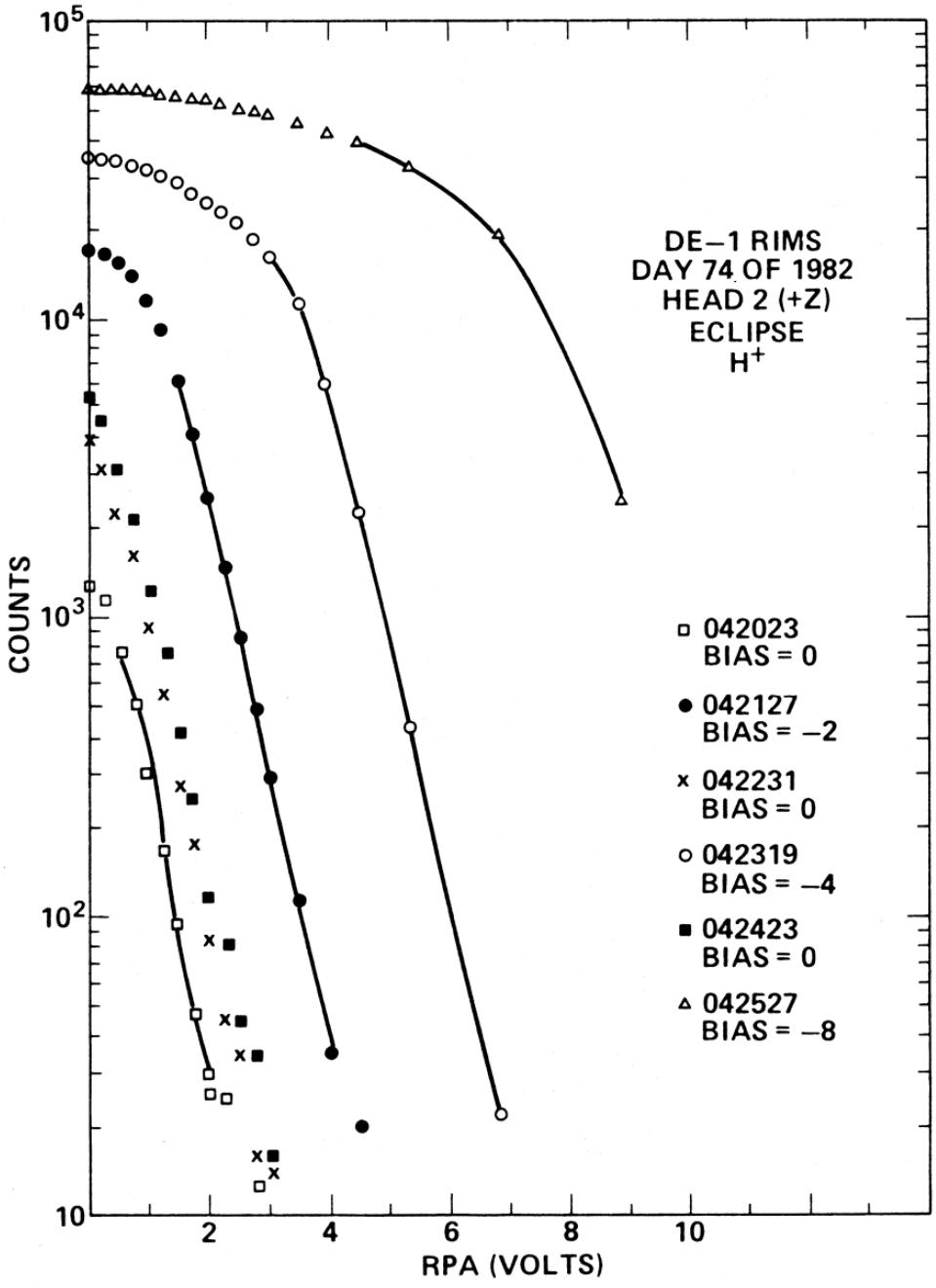

Figure 23. Examples of RPA curves showing the normal effect of increasing aperture plane bias.

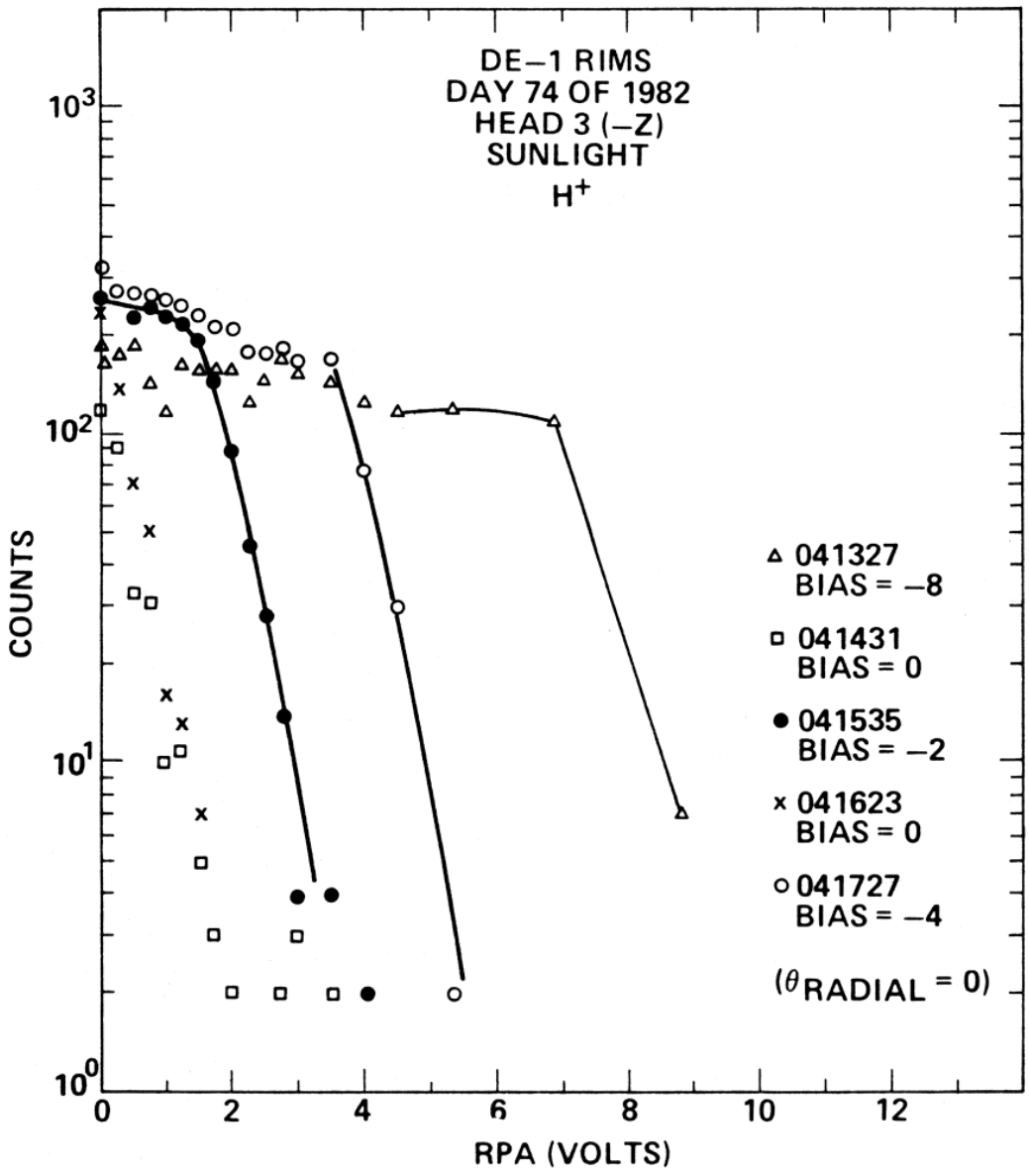

Figure 24. Examples of RPA curves showing abnormal dependence on aperture plane bias.

3. Solution. Limit use of the Z heads to periods with no aperture plane bias applied.

4. Impact on science. -Z head data will be unreliable during bias operations.

H. Summary of Significant Events

This report concludes with a time history of the RIMS operational characteristics, Shown in Table 1.

TABLE 1. TIMELINE OF SIGNIFICANT RIMS EVENTS

Event	Time
Launch	81/215
Initial turn-on at low voltage	81/222
Initial turn-on at high voltage for channeltron conditioning	81/229-81/247
First useful data (+Z head 2-V anomaly present)	81/280
Aperture bias operation	81/287:1927 to 81/288:0200
First oxygen data ("workhorse" mode)	81/292
Radial RPA failure	81/329:195018
First mass scan data	81/364:0700 pass
Radial head RPA temporarily works	81/45:2330 (exits eclipse) to 82/46:0615
-Z head aperture bias failure	before 82/46
+Z head 2-V anomaly ends	82/74:approx. 0300
All heads channeltron bias changed from 2100 to 2400 V	82/160:0006
Radial head channeltron bias changed from 2400 to 2800 V	82/207:1733
Axial heads channeltron bias changed from 2400 to 2800 V	83/064:0535

REFERENCES

1. Fields, S. A., Baugher, C. R., Chappell, C. R., Reasoner, D. L., Hammack, H. D., Wright, W. W., and Hoffman, J. J., Instrument Manual for the Retarding Ion Mass Spectrometer on Dynamics Explorer 1. NASA TM-82484, 1982.

2. Craven, P. D., and Reasoner, D. L., Instrumental Effects on the Temperature and Density Derived from the Light Ion Mass Spectrometer. NASA TM-82536, 1983.

3. Comfort, R. H., Baugher, C. R., and Chappell, C. R., Use of the Thin Sheath Approximation for Obtaining Ion Temperatures from the ISEE 1 Limited Aperture RPA. J. Geophys. Res., Vol. 87, 1982, pp. 5109-5123.

4. Whipple, E. C., Warnock, J. M., and Winckler, R. W., Effect of Satellite Potential on Direct Ion Density Measurements Through the Plasmapause. J. Geophys. Res., Vol. 79, 1974, pp. 179-186.

5. Singh, N., and Baugher, C. R., Sheath Effects on Current Collection by Particle Detectors with Narrow Acceptance Angles. Space Sci. Instrum., Vol. 5, 1981, pp. 295-305.

6. Biddle, A. P., Moore, T. E., and Chappell, C. R., Evidence for Ion Heat Flux in the Light Ion Polar Wind. J. Geophys. Res., Vol. 90, 1985, pp. 8552-8558.

7. Spitzer, L., and Harm, R., Transport Phenomena in a Completely Ionized Gas. Phys. Rev., Vol. 89, 1953, p. 977.

8. Comfort, R. H., Waite, J. H., and Chappell, C. R., Thermal Ion Temperatures from the Retarding Ion Mass Spectrometer on DE 1. J. Geophys. Res., Vol. 90, 1985, pp. 3475-3486.

9. Chandler, M. O., and C. R. Chappell, The Flow of H+ and He+ along magnetic field lines in the plasmasphere. (To be submitted to J. Geophys Res., 1985)

10. Fillius, R. W., Satellite Instruments Using Solid State Detectors. Master's Thesis, State University of Iowa, Dept. of Physics and Astronomy, 1963.

11. Spangenberg, Karl R., Vacuum Tubes. McGraw-Hill Book Co., Inc., New York, NY, p. 347, 1948.

APPROVAL

DE 1 RIMS OPERATIONAL CHARACTERISTICS

By R. C. Olsen, R. H. Comfort, M. O. Chandler, T. E. Moore,
J. H. Waite, Jr., D. L. Reasoner, and A. P. Biddle

The information in this report has been reviewed for technical content. Review of any information concerning Department of Defense or nuclear energy activities or programs has been made by the MSFC Security Classification Officer. This report, in its entirety, has been determined to be unclassified.

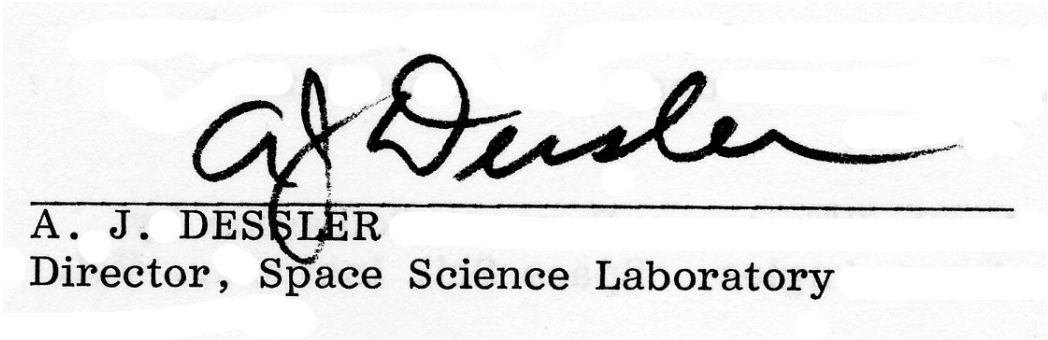

A. J. DESSLER
Director, Space Science Laboratory

U.S. GOVERNMENT PRINTING OFFICE 1985-631-058/20049